---

**Article:**
Yadav, R., Jewell, G., Jones, L.M. et al. (2026) Coupled mechanical-magnetic analysis of cut-edge damage in thin sheet electrical steels. International Journal of Mechanical Sciences, 314. 111375. ISSN: 0020-7403

https://doi.org/10.1016/j.ijmecsci.2026.111375

---

# Coupled mechanical-magnetic analysis of cut-edge damage in thin sheet electrical steels

Rahul Yadav*[1], Geraint W. Jewell[2], Luke M. Jones[1], Hassan Ghadbeigi[1]

[1]School of Mechanical, Aerospace and Civil Engineering, The University of Sheffield

[2]School of Electrical and Electronic Engineering, The University of Sheffield

*r.yadav@sheffield.ac.uk

**Abstract:**

Thin electrical steel sheets are extensively used in electric machine cores owing to their high magnetic permeability and low core losses. Blanking is the predominant manufacturing process for laminations in high-volume applications due to its efficiency and well-controlled parameters; however, localised deformation at the cut edge can adversely affect the magnetic performance. This study systematically examines the influence of blanking on the magnetic behaviour of a non-grain-oriented 3.2% Si electrical steel. The effects of sheet thickness, shear localisation, and fracture mechanisms are investigated through combined experimental and numerical approaches. A novel finite element model is developed for this class of material to directly correlate mechanical deformation with magnetic response, considering blanking-induced strain, strain-rate, and geometric dislocations attributed to non-local effects. A new formulation is introduced to correlate the magnetic permeability with the deformation-induced microstructural changes. In-situ blanking trials with digital image correlation, nano-indentation, and microstructural characterisation were used to validate the model. Magnetic hysteresis and magnetisation measurements using a single-sheet tester reveal that tensile residual stresses markedly reduce permeability, while both tensile and compressive stresses increase magnetic losses through inhibited domain mobility and grain-boundary pinning. The proposed model achieves an over 90% predictive accuracy with experimental measurements, providing a predictive tool for optimising blanking parameters and enhancing electromagnetic efficiency in advanced energy systems.

***Keywords:*** *Blanking, NGO Si-steel, FE model, Plastic deformation, Magnetic degradation*

## 1. Introduction

Electrical steel (ES), also commonly known as Si-steel, is a specialised alloy enriched with silicon, devised for electrical and magnetic applications. The addition of silicon significantly enhances AC magnetic performance primarily by increasing the electrical resistivity but can also led to improvements in magnetic permeability. In the combination these attributes can reduce both hysteresis and eddy current losses [1] making them a preferred material for laminations in transformers, motors, and generators [2]. The formability of these materials is significantly influenced by addition of Si and increased rolling reduction ratio, where the final gauge thickness is reduced to achieve reduced eddy current loss.

Blanking is a widely adopted process for cutting thin sheets due to its efficiency and cost-effectiveness compared to alternative methods such as wire electrical discharge machining [3], water jet cutting, and laser cutting [4,5]. However, the material experiences a large plastic deformation, specifically at the vicinity of the cut edge during the blanking process which introduces residual stress, strain hardening, and microstructural changes. This plastic deformation tends to lead to an increased core loss and reduced permeability, ultimately impacting the magnetic performance of the electric machines and systems [6,7]. The thinner electrical steel laminations lead to improved magnetic performance but at the expense of greater challenges associated in their manufacture. This is partly due to the fact the required die-punch clearances for thinner sheets are increasingly difficult to achieve and maintain throughout long-term operation. Therefore, a thorough understanding and prediction of the functional performance of the stamped laminations is critical for optimising their application in advanced technological systems.

Electrical steels are nominally formed with only a few grains across their thickness [8,9]. Therefore, their blanking performance, and its subsequent effects, are not only affected by factors such as punch force, clearance, tooling design, and material properties, but also by the intrinsic microstructural characteristics of the material, particularly grain and grain boundaries [10]. The microstructural effect becomes more significant in thinner sections as there are one to two grains to accommodate the applied local plastic deformation during the blanking process. The plasticity induced microstructural evolutions could lead to strain-induced phase transformations as well as significantly influencing magnetic behaviour [11]. Local magnetic properties, including magnetic losses and the magnetisation force, at the cut edge are reported to differ sometimes markedly, from the bulk properties due to increased hardness, microstructural changes, and dislocation interactions at grain interiors and boundaries [12, 13].

The magnetic losses, including magnetic hysteresis loop, magnetic permeability and coercivity are usually measured using the single strip tester in accordance with IEC 60404-3, wherein a single strip of electrical steel is subjected to magnetic induction under a DC current [14,15]. In this context, the effect of residual stresses on magnetic behaviour was evaluated using SST by analysing hysteresis loops, magnetic permeability, and magnetisation curves. The observed changes were attributed to the generation of new peening sites by the introduction of residual stresses, which contributed to an increase in coercivity. [16]. It is reported that for a 0.35mm thick electrical steel, the blanking induced deformation results in a 35% reduction in magnetic permeability (measured on ring samples) while the hysteresis losses increased by 20 % after blanking [17]. The magnetisation properties deterioration has a direct correlation with the grain size and is inversely linked to the width of the samples. This is attributed to dimensional effects that introduce additional magnetic anisotropy, consequently leading to a reduction in magnetic permeability [18]. The interplay between grain size, sheet thickness and magnetic performance is an area of growing research interest, particularly in the development of components for electrical and magnetic applications.

Blanking processes have been extensively investigated using both analytical and numerical modelling approaches. Analytical equations, reported by [19,20], have been developed to predict the forces required and the fracture mechanisms involved during materials separation. In parallel, numerical finite element models have been employed to simulate material behaviour during the shearing process, providing insights into local plastic deformation and the quality of the blank at the cut edge [21,22]. To achieve these predictions, a range of damage and fracture models have been employed. These include empirical models such as the Cockroft-Latham criterion [23], which account for the effects of stress triaxiality, as well as phenomenological models that incorporate the physics of ductile damage in materials, such as void nucleation, growth, and coalescence [24, 25]. Moreover, the influence of both compressive and tensile principal stresses has been explicitly considered in more recent formulations. Lemaitre damage model [26,27], which introduced damage evolution as a function of plastic strain and stress state, provided a robust framework for capturing the progressive degradation of material stiffness and strength during the blanking process [26,27]. All these models are either based on limited range of stress states or rely on material constants that are complex and require substantial effort to calibrate.

Blanking research and modelling of its fracture mechanics has predominantly focused on various grades of steels including automotive-grade steels [28], Bainitic Ferrite (TBF) and

TRIP steels [29,30], as well as other aluminium alloys [31]. Although a few studies have examined the blanking of electrical steels [32,33], most have primarily focused on modelling mechanical deformation and have not conducted a comprehensive investigation of the coupled mechanical and magnetic effects. The magnetic properties of electrical materials, such as permeability, coercivity, and magnetic losses, are known to be very sensitive to mechanical stresses, especially induced from plastic deformation, due to the introduction of additional dislocations, residual stresses, and strain-induced anisotropy. It is known that elastic tensile stresses aligned with the magnetic domain enhance the magnetisation properties, while compressive elastic stresses have a hinder magnetic domain motion. In contrast, any plastic deformation, both tensile and compressive, tend to reduce magnetisation loss [34,35]. The effect of small plastic deformation (<1%) on magneto strictive responses of ferro magnetic polycrystalline material NO-3% Si-Fe was simulated using coupled micromechanical plastic hardening with magneto-elastic formulations and validated the degradation of magnetic susceptibility [36,37]. Pengpeng [38] introduced a magneto-elastoplastic coupling model incorporating magnetic field, applied stress, and plastic deformation through an equivalent field method, though no experimental validation was provided. In a separate study, the effect of larger plastic strains (up to 3%) and reloading stresses on magnetization and magnetostriction was simulated using a macroscopic model using kinematic hardening parameters [39] with results compared to experimental measurement. The effect of mechanical stress on magnetic behaviour has recently been studied using the two-domain model which introduces effective pinning energy to accurately capture the strain-dependent magnetic permeability of anisotropic grain-oriented steels [40]. Extended Jiles–Atherton hysteresis model [41] uses Gaussian-distributed parameters to reflect the magnetic response of quenched and tempered steels more realistically. These studies provide novel frameworks for predicting magnetic properties under operational conditions, offering improved insight into the interplay between mechanical strain and magnetisation.

Although attempts have been made to model the interaction between mechanical stresses and magnetic properties, these do not consider spatial variations due to the cut edge defect and local magnetic damage on the blank parts. To the best of the authors' knowledge, the complex interaction between the severe plastic deformation regime observed during blanking of laminations and its effect on the magnetic response of electrical steels has received little attention in the literature and is particularly under-reported for thin-gauge materials, which are highly sensitive to deformation and microstructural changes. Additionally, the role of residual

stress states and their evolution under dynamic high-strain-rate loading conditions have not yet been adequately modelled or experimentally validated in electrical steels.

This study aims to address the gap in the current state of the art related to the interplay between mechanical and magnetic behaviour after blanking process for thin sheet electrical steel laminations. A novel coupled model is proposed to predict the blanking induced magnetic damage, including hysteresis losses and permeability, in a 3.2% Si non- grain oriented (NGO) electrical steel. An integrated mechanical–magnetic characterisation framework is introduced that combines experimental damage assessment with a multiscale modelling approach. The model captures strain localisation and incorporates the effects of geometrically necessary dislocations (GNDs), which arise from severe strain gradients developed during sheet blanking. The subsequent effect of these deformation mechanisms on magnetic permeability is then evaluated, establishing a mechanistic understanding of magneto-mechanical coupling. The dependency of magnetic permeability on strain-induced microstructural features is explicitly considered. The modelling results are systematically validated using a combination of DIC for strain field mapping, EBSD for microstructural characterisation, and corresponding magnetic measurements obtained from the previous studies by the authors.

## 2. Methodology

A combined experimental-numerical modelling approach was adopted in this study. The experimental investigations were aimed at understanding the mechanical properties of the material studied as well as quantifying the effect of blanking induced defects on magnetic performance. A predictive model was developed to establish a link between the plastic deformation observed in blanking with the measured magnetic performance losses. This section provides a detailed description of the experimental methods and modelling approach.

### *2.1 Experimental setups*

#### *2.1.1 Mechanical properties characterisation*

Cold-rolled thin silicon steel (Si-steel) sheets with a thickness of 0.2 mm and 0.35 mm were used in this study. The material contained a nominal 3.2% silicon and were classified as non-grain-oriented grades NO20 and NO35 [42]. To determine the effect of rolling direction on the mechanical properties, including plastic deformation and fracture, tensile tests were conducted in both the rolling (RD) and transverse (TD) directions (Fig. 1(a)). The effect of stress state on fracture, i.e. stress triaxiality, was captured using tensile specimens. Different notch geometries were used to achieve a range of positive stress triaxiality values as shown in (Fig. 1(b,c)), while

the shear failure properties were determined using a butterfly geometry (Fig. 1(d). Uniaxial tensile tests were conducted at a crosshead speed of 10 mm/min under room temperature conditions using a 25 kN electro-mechanical Tinius Olsen H25KS. Full field non-contact DIC technique was employed to capture both local and global strain distributions across the specimens, providing a comprehensive assessment of the material's mechanical response under loading conditions. A reference image is compared with a deformed image, and the resulting relative deformation is used to calculate strain. A sensitivity study was carried out to determine the most suitable DIC parameters. This led to the selection of an accurate configuration using a subset size of 23 pixels (0.55 mm) and a step size of 9 pixels (0.21 mm) for processing the captured images.

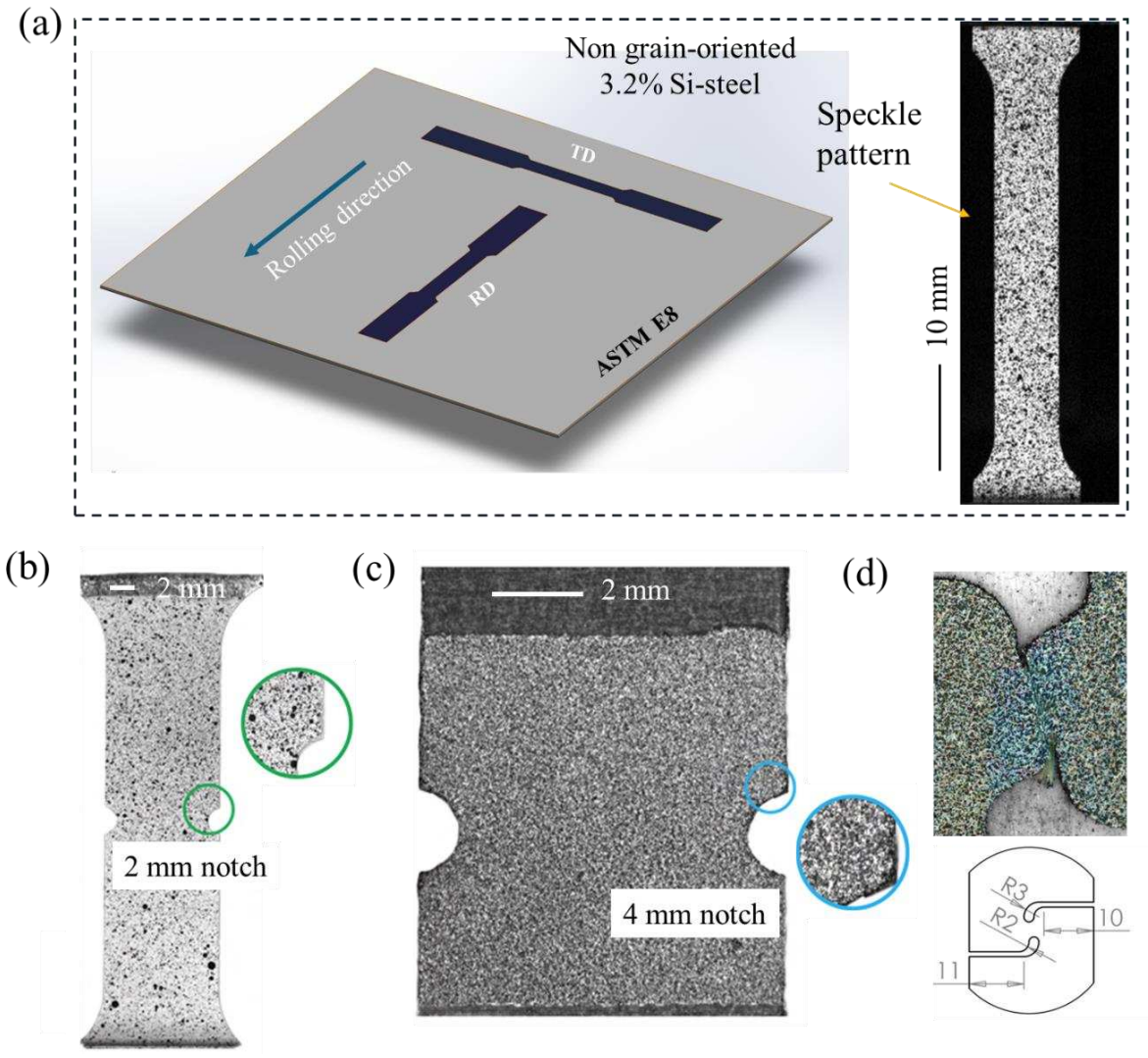


**Fig. 1:** Gauge geometry of samples used for: **(a)** uniaxial tensile specimen prepared with speckle patterns for DIC measurements; **(b)** notched specimen with a 2 mm notch radius; **(c)** notched specimen with a 4 mm notch radius, both used to achieve different levels of triaxiality; and **(d)** shear specimen [43], (all the dimensions are in mm unit).

### *2.1.2 Blanking experiments*

The blanking experiments were carried out using two distinct die sets to assess the influence of blanking parameters on local deformation and magnetic performance. Fig. 2(a) presents a schematic and exaggerated illustration of the blanking setup. The punch moves towards the sample while the blank holder keeps the sample in position and restricts lateral deformation to shear a metal sheet against a die. This system facilitated real-time tracking of the cutting process and localised deformation of the material. Die Set-I featured an open-sided configuration, allowing the integration of an in-situ high-speed DIC system (Fig. 2 (b)). Fig. 2(c) shows the in-situ blanking setup highlighting the deformation zone in which the local strain maps were calculated. Die Set-II was a closed-type die set, used to produce 50 mm ×10 mm blank section for further magnetic characterisation in both the Rolling Direction (RD) and the Transverse Direction (TD) as explained in [42] for producing rectangular blanks measuring.

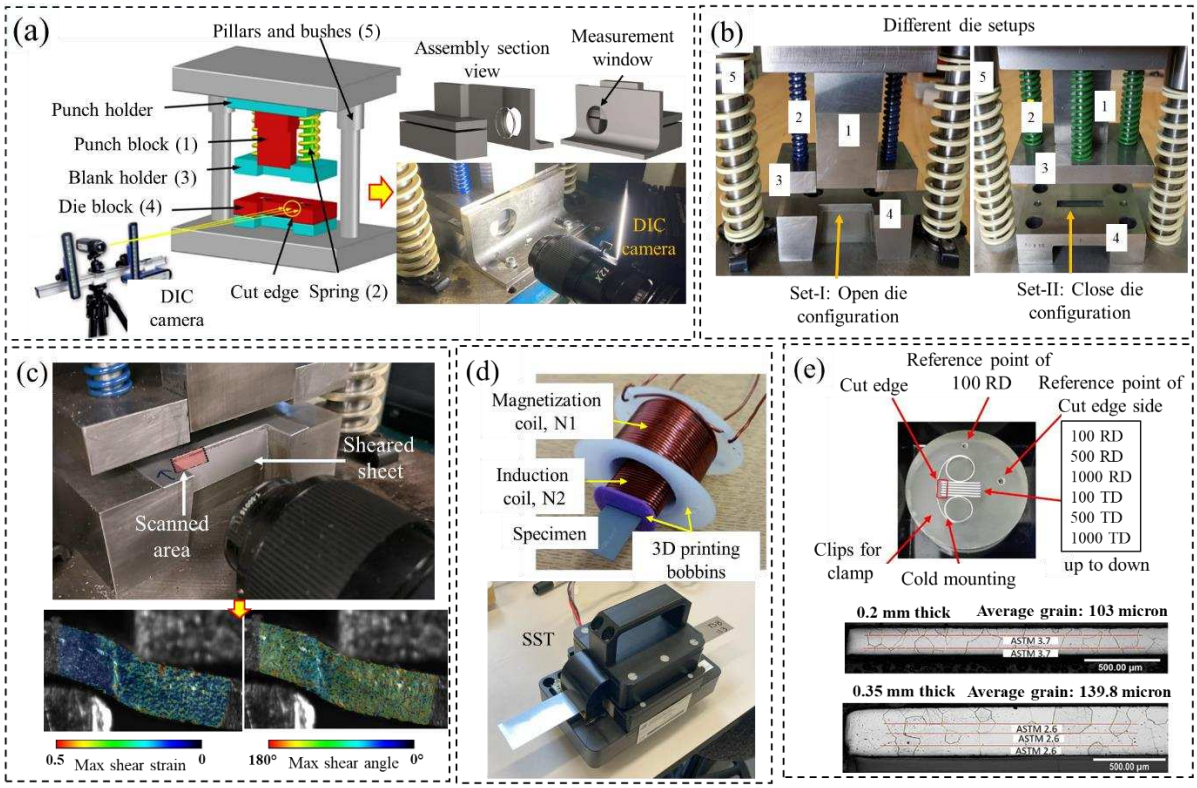


**Fig. 2: (a)** Schematic illustration of the experimental blanking die set with the DIC setup; **(b)** Die configurations (open and closed) employed in the analysis; **(c)** DIC images providing an exaggerated view of the blanking process, highlighting deformation characteristics within the domain of interest; **(d)** single-sheet tester setup design for magnetic flux measurement, analogous to the standard SST; **(e)** blanked samples of 0.2 mm and 0.3 mm thickness mounted in cold-mount resin for SEM imaging of the cut edge [42].

This setup was specifically utilised to investigate the impact of blanking parameters on the resultant magnetic performance. The blanking experiments were conducted at varying

displacement rates, 100, 500 and 1000 mm/min with die clearance set to 10% of sheet thickness. The test speeds fall within the lower to mid-range used in industry, and a 10% die clearance is a common choice. That said, both speed and clearance depend on the material and press, so factors like press type, lubrication, material behaviour, therefore results may not transfer directly to high-speed or large-scale production work.

*2.1.3 Magnetic properties characterisation*

Magnetic properties of electrical steels are typically measured using techniques such as the Epstein frame, single sheet tester (SST), and ring tester [44]. These tests measure aggregated magnetic properties over the full sample or a substantial and defined portion of the sample in accordance with standards such as IEC 60404-3:2022. However, these methods generally require large samples (orders of 200-300 mm long), making them less suitable for investigating localised phenomena such as cut-edge defects, where only small regions of the material are affected and the phenomena of interest can be swamped by the large unaffected material region which is remote from the regions of interest. To address this limitation, Ghali Al-Rubaye [45] developed a novel a mini–Single Sheet Tester (m-SST), allowing precise magnetic characterisation of localised regions with modest material requirements. The normal induction curve was obtained while providing the required magnetisation field strength using a double-yoke configuration (Fig. 2(d)), which provided a near-closed magnetic circuit, reduced eddy current formation, and ensured minimal self-demagnetising effects. The tester fixture is designed to accommodate the flat, rectangular blanked specimen (50×10 mm), with the distance between the pole faces of the double-yoke measuring 30 mm. It is recognised that this m-SST is not compliant with the standard dimensions set out in IEC 60404-3:2022, being considerable smaller although having similar proportions. As noted in [45] and [46] calibration can be performed by carefully producing miniature samples from standard strip samples that have been previously measured in accordance with the published standards.

The maximum magnetic flux was compared for different cut edges. Following magnetic testing, the samples cut edge sections were mounted in cold-mount resin (Fig. 2(e)). The average grain size was measured to be 103 μm for the 0.2 mm thick sheet and 139.8 μm for the 0.35 mm thick sheet. The characterisation of the cut edge sections was performed using multiple techniques. Scanning Electron Microscopy (SEM) imaging was employed to examine the morphological characteristics of the edges, while nano-hardness measurements provided insights into the mechanical properties of the shear-affected zone. Additionally, Electron Backscatter Diffraction (EBSD) analysis was conducted to assess the microstructural features,

including grain orientation and grain boundary characteristics. The EBSD examination was carried out with a step size of 0.5 μm using a JEOL FEG SEM 7800F, which was equipped with an Oxford Energy Dispersive Spectroscopy (EDS)/EBSD system [42].

To further evaluate the microstructural distortions induced by blanking, Geometrically Necessary Dislocation (GND) maps at the cut edge were generated following the methodology outlined in references [47-48]. Nano-indentation tests were performed using a Berkovich indenter, applying a maximum load of 5 mN with a dwell time of 15 seconds. The experimental analysis encompassed all sample groups, categorized based on their thickness and deformation plane. These groups were designated as 0.2RD, 0.2TD, 0.35RD, and 0.3TD, representing variations in thickness and directional blanking influences. The comprehensive assessment of these parameters provided critical insights into the interplay between blanking conditions and resultant material properties, with a particular focus on mechanical and magnetic characteristics.

### *2.2 Coupled finite element model development*

#### *2.2.1 Model setup*

The ABAQUS-Explicit finite element package was used to develop a numerical simulation of the blanking process. The modelling approach is illustrated in the flowchart shown in Fig. 3(a) and the equations developed are described in the following section. The FE model replicates the banking set-up arrangement with the die and blank holder restricted in both translational ($U_{x,y,z}$) and rotational ($\Omega_{x,y,z}$) degrees of freedom, simulating rigid supports (Fig. 3(b)). The punch is restricted in the X and Z directions but allowed to move downward along the Y-axis, applying the blanking load. These conditions ensure the process involves only shearing and compression along the Y direction. The element sizes gradually increase from the critical regions with high stress and deformation localisation, i.e. the clearance zone, towards the bulk of the sheet to optimise computational effort without compromising unduly accuracy. Structured elements with thermal degrees of freedom (CPE4T and C3D8T), each with a size of 1 micrometre, were employed in the clearance zone to enable a coupled dynamic temperature–displacement analysis. This approach accounts for the significant plastic deformation and potential temperature rise occurring during the blanking process. The punch and die were considered as rigid bodies with a measured punch edge radius of 10 μm and 12 μm, respectively. The sliding friction formulation was incorporated at the interfaces between the punch-die, blank holder-sheet, and die-sheet. The punch and die made of the Tool steel,

therefore, the friction coefficient between the sheet and punch was set to 0.48 based on pin-on disc test measurements.

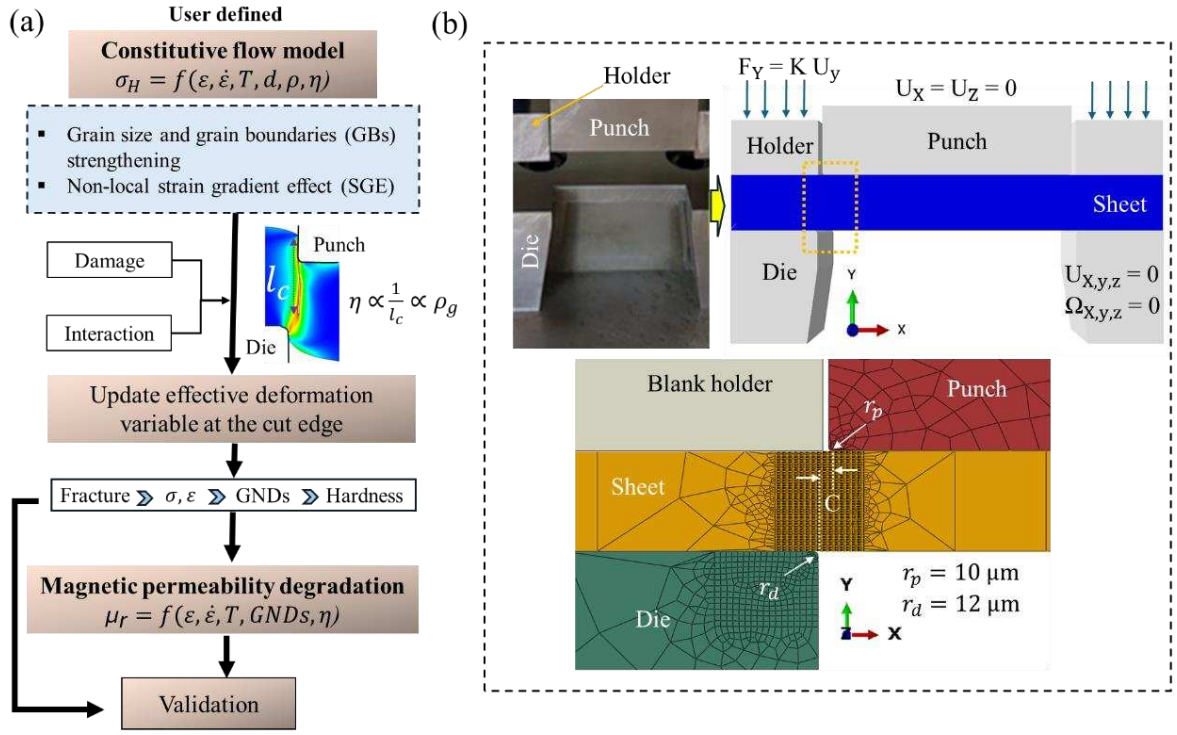


**Fig. 3: (a)** Flowchart illustrating the overview of model development **(b)** finite element assembly model and boundary conditions based on the experimental setup and Meshed topography of the punch-die-sheet assembly, with a refined mesh applied in the cutting zone.

*2.2.2 Material model for thin sheet electrical steel with 3.2% Si*

During blanking, the material experiences high strain rates, large plastic deformation, and possible temperature effects, and therefore the Johnson-Cook (JC) model [49] was chosen to capture strain hardening, strain rate sensitivity, and thermal softening. There are only a very few individual grains through the thickness of the sheet, hence grain structures and boundaries present in the clearance region significantly affect the plastic deformation and strain hardening in this region. To reflect this, the original JC model was extended in this study to incorporate grain size-dependent term ($\frac{k_y}{\sqrt{d}}$) to account for Hall–Petch strengthening and classical strain hardening ($B\varepsilon^n$) in Eq. 1, thereby accounting for the microstructural effects [50,51].

$$\sigma_{GBs} = \left[A_0 + \frac{k_y}{\sqrt{d}} + B\varepsilon^n\right]\left[1 + C ln(\frac{\dot{\varepsilon}}{\dot{\varepsilon}_0})\right]\left[1 - \left(\frac{T - T_0}{T_0 - T_{melt}}\right)^m\right] \quad (1)$$

$$A_0 = 2Gb\sqrt{\rho} \quad (2)$$

Where $A_0$ and $k_y$ are the intrinsic strength and strengthening coefficient of the material. These model parameters were obtained by experimental measurements of grain size and dislocation

density of the blanked samples. *G* and *b* are shear modulus and Burgers vector. The mechanical work during the blanking experiments is a dominant mechanism for grain refinement over temperature-induced mechanisms. This is due to the short duration and small thickness of the material, which does not result in significant localised heating. Therefore, it was assumed that the average grain diameter *(d)* is considered to reduce from $d_0$ with plastic deformation under high strain rate and temperature. Q and R are activation energy (KJ/mol) and universal gas constants (J/mole) respectively.

$$d = d_0 \, \dot{\varepsilon}^{-m_1} \, exp\,(-\frac{\zeta Q}{RT}) \tag{3}$$

Furthermore, the clearance, punch, and die radius are of a similar scale and cut through only a few grains in the thin sheet. This leads to the build-up of additional dislocations, known as geometrically necessary dislocations (GNDs), which influences the material's response by introducing additional hardening. This increased resistance to deformation, causes thin sheets to exhibit greater strengthening than predicted by conventional material models that account only for statistically stored dislocations (SSDs) arising from random dislocation interactions. The GNDs are required to accommodate strain gradients in regions of non-uniform deformation, known as non-local effects, particularly near the punch contact areas during blanking. These effects are characterised by a length scale [52], denoted as $l_c$, during blanking. The statistically stored dislocation density ($\rho_s$) arises from plastic deformation rather than from geometric constraints. The dependence of the modified flow model on SSDs and GNDs is described in Eqs 4 and 5, are accounted for using the user-defined subroutine VUHARD.

$$\sigma_{eff} = \sigma_{GBs}\sqrt{1 + r'\frac{\rho_g}{\rho_s}} \tag{4}$$

$$\rho_g = \frac{\kappa \epsilon_{ij}}{b l_c} = \frac{\kappa \eta}{b} \tag{5}$$

Where $r'$ is the magnitude of Nye tensor, $\epsilon_{ij}$ is the shear strain, $\kappa$ is the edge factor, $\rho_s$ and $\rho_g$ are statistically and geometrically stored dislocations. Consequently, the flow stress associated with meso-scale deformation, particularly that influenced by grain boundaries ($\sigma_{GBs}$), as expressed in Eq. 1 through the coupling of the JC model and the Hall–Petch relationship, can be equated to the dislocation-based flow stress described by Taylor's theory [53,54]. The resulting expression is presented in Eq. 6. The final flow stress is presented in Eq. 7, where GNDs and non-local influence are included [55,56]. The model constants M, $\eta$, are Taylors' factor and strain gradient.

$$\rho_s = \left(\frac{\sigma_{GBs}}{M\alpha\, G}\right)^2 \tag{6}$$

$$\sigma^e_{SGE} = \sqrt{{\sigma_{GBs}}^2 + r'\eta b(M\alpha\, G)^2} \tag{7}$$

The flow stress–strain curves in Fig. 4(a) illustrate the multiscale constitutive approach used in the simulations. Three models are compared to show the influence of different microstructural mechanisms. The results highlight that grain boundary strengthening (linked to grain size and dislocation density) and nonlocal effects (SGE effects) significantly delay damage initiation and enhance the predicted flow stress. This multiscale approach effectively connects grain-level behaviour with the overall material response, offering a robust framework for accurately simulating the blanking process.

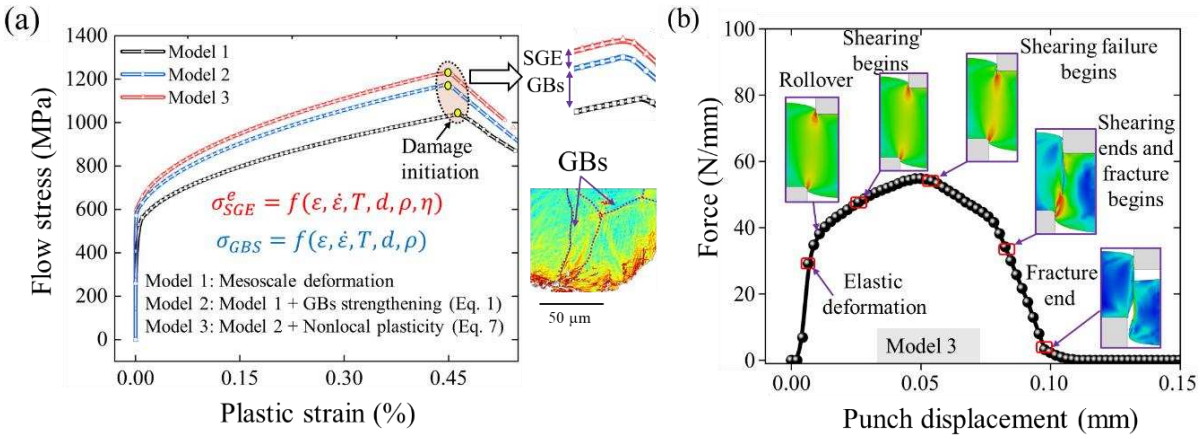


**Fig. 4**: **(a)** Flow stress–strain responses for three constitutive models incorporating mesoscale deformation, grain boundary strengthening, and nonlocal plasticity **(b)** punch force evolution during thin sheet blanking simulated using Model 3, highlighting key stages of deformation and failure, including rollover, shearing, and fracture.

Fig. 4(b) shows the evolution of punch force during a thin sheet blanking simulation. The force–displacement curve highlights the key stages of deformation and failure, beginning with elastic deformation, followed by the onset of shearing and the formation of rollover. As the punch continues to move, shearing failure sets in and eventually results in the complete fracture of the sheet. These distinct stages are illustrated through contour plots positioned along the curve, offering a clear visual depiction of how the deformation becomes increasingly localised and ultimately leads to fracture during the blanking process.

### *2.2.3 Damage and fracture modelling*

A progressive damage model is used to capture material failure by gradually reducing stiffness as damage develops. The shift from plastic deformation to fracture is represented by element deletion once a critical damage limit is reached, allowing the simulation to reflect material

separation and crack formation realistically [57]. A material separation criterion was defined by incorporating a damage initiation and evolution model. Ductile damage initiation criterion was used wherein damage accumulation parameter ($\omega$) is defined as a function of the equivalent strain ($\varepsilon_{\boldsymbol{e}}{}^{pl}$), stress triaxiality ($\eta$) and strain rate ($\dot{\epsilon^{pl}}$) in Eq. 8.

$$\omega = \int \frac{d\varepsilon_{\boldsymbol{e}}{}^{pl}}{\varepsilon_i\left(\eta, \dot{\epsilon^{pl}}\right)} \tag{8}$$

This was based on the observations of ductile fracture at the cut edge as reported in [42]. An exponential damage evolution based on critical displacement to fracture was also implemented to simulate fracture propagation and account for the progressive loss of material stiffness as the damage evolves. This is to reflect the real-time degradation (Eq. 9), where $l$ represents the minimum size of elements, $\beta$ is the exponential degradation coefficient, and $u_f$ is the displacement at fracture.

$$D = \frac{1 - e^{-\beta\left(\frac{l\,\varepsilon_{\boldsymbol{e}}{}^{pl}}{u_f}\right)}}{1 - e^{-\beta}} \tag{9}$$

Stress triaxiality, strain at damage initiation and fracture were extracted from the experimental phase of the study explained in section 3.1 using DIC techniques employed to capture the localised strain fields within the material during deformation.

*2.2.4 Hardness at the cut edge*

Hardness increases due to the strain hardening effect in the metallic materials, therefore hardness and flow stress are both linked to the resistance of materials to plastic deformation, although they pertain to different mechanical contexts. Despite these contextual differences, both properties are fundamentally governed by similar deformation mechanisms, particularly the motion and interaction of dislocations [58]. In this study, the initial surface hardness ($H_0$) was experimentally measured prior to cutting, while the subsequent increase in hardness was estimated through FE simulation using locally determined flow stress of the material. The resulting relationship is presented in Eq. 10.

$$H = H_0 + k_0\,\sigma^{e}_{SGE} \tag{10}$$

*2.2.5 Modelling of permeability and blanking-induced degradation*

Plastic deformation resulting from intense shearing and fracture at the cut edge leads to significant changes in the microstructure and mechanical properties of the material in the vicinity of the cut edge. Such severe deformation could lead to the accumulation of dislocations

along grain boundaries and microstructural damage within the shear-affected zone that locally disrupts magnetic domain alignment, leading to a reduction in magnetic permeability [59]. The reduction in permeability, a key indicator of magnetisation capacity affected by blanking, is used as a measure to assess material degradation here. Temperature rise in blanking is expected to be well below the Curie temperature (700-750 °C), hence having a minimal effect on the magnetic properties of materials. Therefore, only mechanical deformation predicted by the developed model was considered in order to simulate dislocation and microstructural alterations for the prediction of the blanking-induced permeability changes. A mathematical relationship describing the variation of permeability with plastic deformation during the blanking process has been proposed and developed in this study, as presented in Eq. 11. This formulation is suitable for mechanically based cutting processes occurring within highly localised zones where non-local effects are significant.

$$\mu_r = \mu_{ro} \times exp\left(-\alpha_o\left(\varepsilon^n + L\sqrt{\rho_{gnd}}\right)\left(1 + q\, ln\left(\frac{\dot{\varepsilon}}{\dot{\varepsilon}_o}\right)\right)\right)\left(\frac{T_c - T}{T_c - To}\right)^{mo} \quad (11)$$

where $\mu_r$ is the relative permeability after cut, $\mu_{ro}$ is the permeability before cut, $\varepsilon$ is the plastic strain, $\rho_{gnd}$ is the GND density, $\dot{\varepsilon}$ is the strain rate, and $T$ is the local temperature and $T_c$ is the curie temperature. The parameters $\alpha_o$, $n$, L, q, and $m_0$ are material-specific constants. Model parameters were obtained from uniaxial and blanking experiments, with DIC measurements providing quantitative data on material behaviour under both static and high strain-rate conditions, ensuring accurate representation for simulation models. The model constants used in the simulation are listed in Table 1. In the simulation, the magnetic flux density (B) is determined using a linear approximation of the unsaturated region of the initial magnetisation curve of ferromagnetic materials. This linear approximation allows the use of the Eq. 12, where B is the magnetic flux density (T) and H is magnetic strength (A/m).

$$B = \mu_o \mu_r H \quad (12)$$

The total magnetic power loss, representing the energy dissipated per unit mass of material during cyclic magnetisation, arises from two main mechanisms, hysteresis loss and eddy-current loss [60,61]. The hysteresis loss is associated with the energy expended through the irreversible movement of magnetic domain walls within the material, whereas the eddy-current loss results from circulating currents induced in the laminations by the time-varying magnetic field. The total loss $(P_l)$ can be estimated using the extended Steinmetz expression, which combines both contributions using the Eq. 13 [62]. In this expression, $K_h$ is the Steinmetz

hysteresis coefficient (material-dependent) expressed in *W/(kg·Hz·T)*, $K_e$ is the eddy-current loss coefficient in *W/(kg·Hz²·T²)*, $f$ is the frequency of magnetisation in *Hz*, $B_m$ is the peak magnetic flux density in *T*, and *z* is a material specific constant.

$$P_l = K_h f {B_m}^z + K_e f^2 {B_m}^2 \quad (13)$$

It should be noted that, the permeability is determined from the initial magnetisation curve, corresponding to the slope of the B–H curve in the region before the onset of any appreciable saturation. This was obtained experimentally, measured up to a magnetising field of approximately 200 A/m, where the B–H response remains close to being reversible and single-valued. Beyond this low-field range, hysteresis becomes significant, and permeability is no longer uniquely defined. To model the nonlinear and hysteretic behaviour at higher fields, a phenomenological power-loss formulation was applied which empirically captures both hysteresis and eddy-current effects as a function of frequency and induction amplitude.

**Table 1.** Model parameters for assessing magnetic permeability and power loss of NGO 3.2% Si-steel

| | $\alpha_o$ | $q$ | $m_0$ | $n$ | $\dot{\varepsilon}_o$ | $K_h$ | $K_e$ | $z$ |
|---|---|---|---|---|---|---|---|---|
| 0.2 mm | 0.47 | − 0.068 | 0.9 | 0.384 | 0.025 | 0.0105 | 0.0003 | 1.6 |
| 0.35 mm | 0.7 | − 0.063 | 0.9 | 0.348 | 0.025 | 0.0102 | 0.00028 | 1.6 |

## 3. Results and discussion

### *3.1 Mechanical response in thin sheet testing*

The distribution of maximum normal strain in the thin sheet samples is shown in Fig. 5(a) for (i) undeformed conditions to assess the DIC accuracy measurement and (ii-iv) during the tensile tests and (v) immediately prior to fracture, highlighting localised necking behaviour. The 0.35 mm thick sheet exhibited a higher maximum normal fracture strain compared to the 0.2 mm sheet, which attributed to the greater number of grains through the thickness, allowing for more homogeneous plastic deformation and improved strain accommodation during loading. The difference in grain population affects the activation and motion of dislocations, leading to delayed onset of necking and fracture in the thicker sheet. Fig. 5(b) presents the true stress–strain curves for both 0.2 mm and 0.35 mm sheets in the rolling and transverse directions. The yield strength is determined to be 310 ± 21 MPa for the 0.2 mm sheet and 368 ± 15 MPa for the 0.35 mm sheet (Fig. 5(c)). The increase in yield strength with thickness may be attributed to size effects and associated microstructural differences such as grain size and orientation distributions.

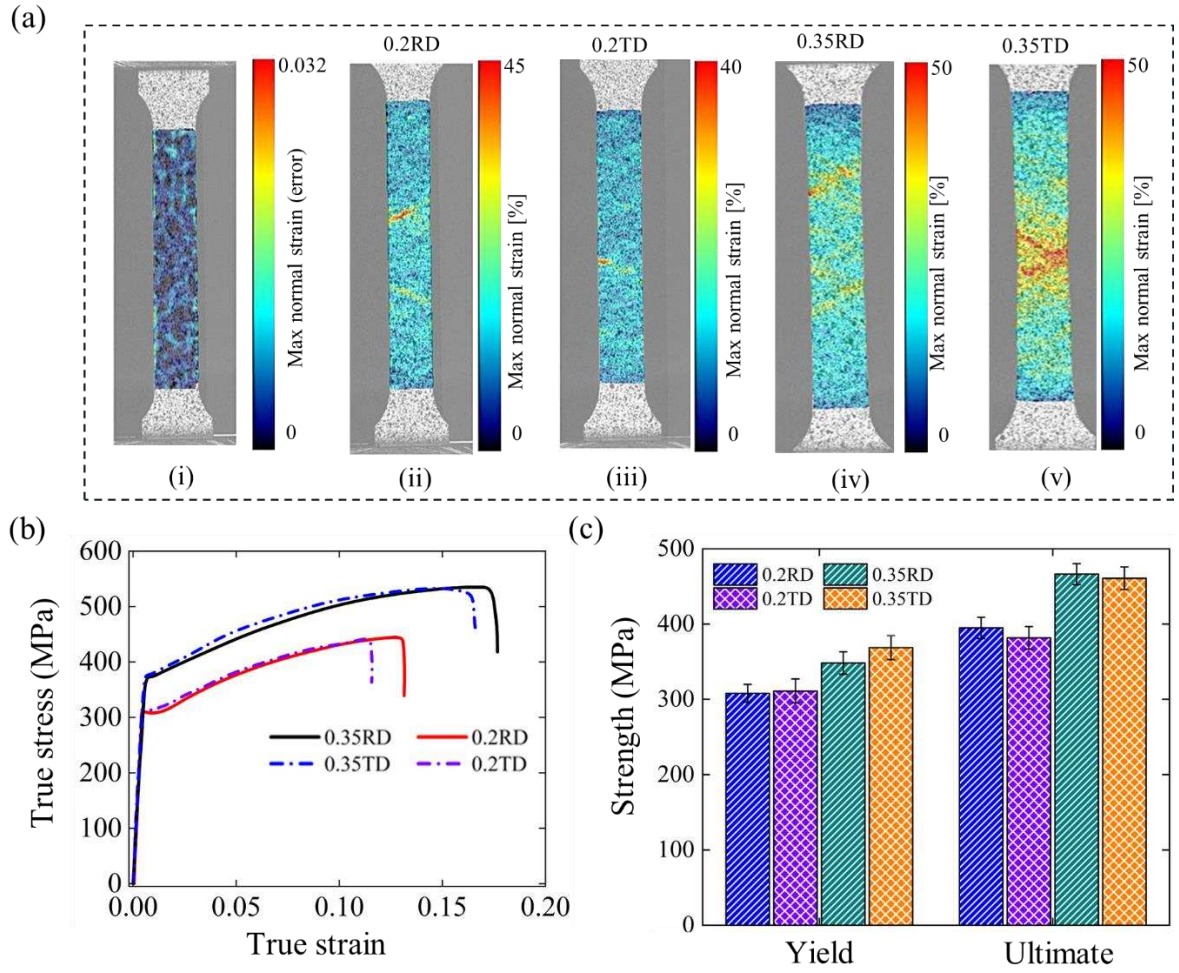


**Fig. 5: (a)** Normal strain distribution measured via DIC shows: (i) the baseline error in the undeformed state, and (ii–iv) the strain distribution immediately before fracture **(b)** true stress–strain curves for various sheet thicknesses at a crosshead speed of 10 mm/min; **(c)** ultimate tensile strength and yield strength for different thicknesses of NGO 3.2% Si-steel.

Higher strain at fracture was measured during the shear tests as it is demonstrated in Fig. 6(a). The onset of damage and the final fracture strain were quantified using DIC by tracking strain localisation and crack initiation points. These values are summarised in Fig. 6(b), providing critical input data for failure modelling and simulation of forming/blanking processes. The results show that stress triaxiality ($\eta_{tr}$) has a significant effect on fracture strain. The shear sample, which experiences zero stress triaxiality, exhibited the highest fracture strain of 1.2, indicating large deformation before failure. In contrast, the notched samples, with higher triaxiality values of 0.445 for the 2 mm notch and 0.34 for the 4 mm notch, showed lower fracture strains of 0.6 and 0.44 respectively. This trend confirms that increased stress triaxiality promotes earlier fracture, reducing the material's ductility. Interestingly, the smaller 2 mm notch, despite having a higher triaxiality than the 4 mm notch, had a higher fracture strain,

likely due to differences in stress concentration effects. Overall, the data highlights that as triaxiality increases, the material becomes more susceptible to brittle failure.

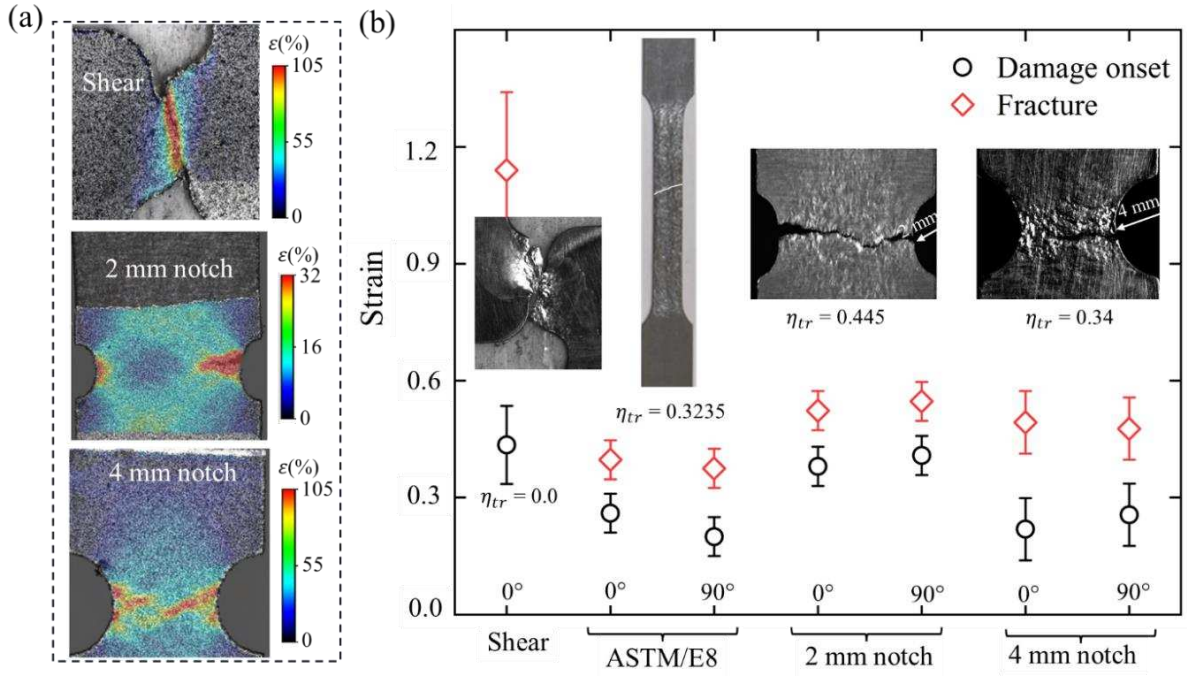


**Fig. 6: (a)** Strain distribution measured using DIC immediately prior to fracture for the 0.2 mm thick sheet **(b)** the plot compares strain at damage onset and fracture for 0° and 90° orientations under varying stress triaxialities ($\eta_{tr}$), highlighting the influence of geometry and loading direction on ductile failure.

### *3.2 Mechanical response in thin sheet blanking*

Fig. 7(a) illustrates sequential frames, recorded at 10 Hz, from the in-situ blanking process, highlighting the evolution of deformation leading to fracture. In frame 4, the formation of a shear band is evident, marked in yellow. This localised shear significantly weakens the material along the band, facilitating sample edge rotation. As deformation progresses, this rotation contributes to the development of a tension-dominated region. Ultimately, this promotes crack initiation and propagation along the path indicated by the white line in frame 6, a direction distinct from the shear band orientation, resulting in material fracture. Fig. 7(b, c), the strain development during the blanking process was tracked in real time using in-situ DIC for sheet thicknesses of 0.2 mm and 0.35 mm. Each set of images (frames 1–4) captures key stages of deformation leading up to fracture. The colour maps represent local strain values, ranging from 0% to over 120% (red), as shown in the scale bar. In both cases, strain begins to concentrate near the edge where the punch contacts the sheet. By the final frame (4), the strain becomes highly localised, especially in the 0.35 mm sheet signalling the onset of fracture.

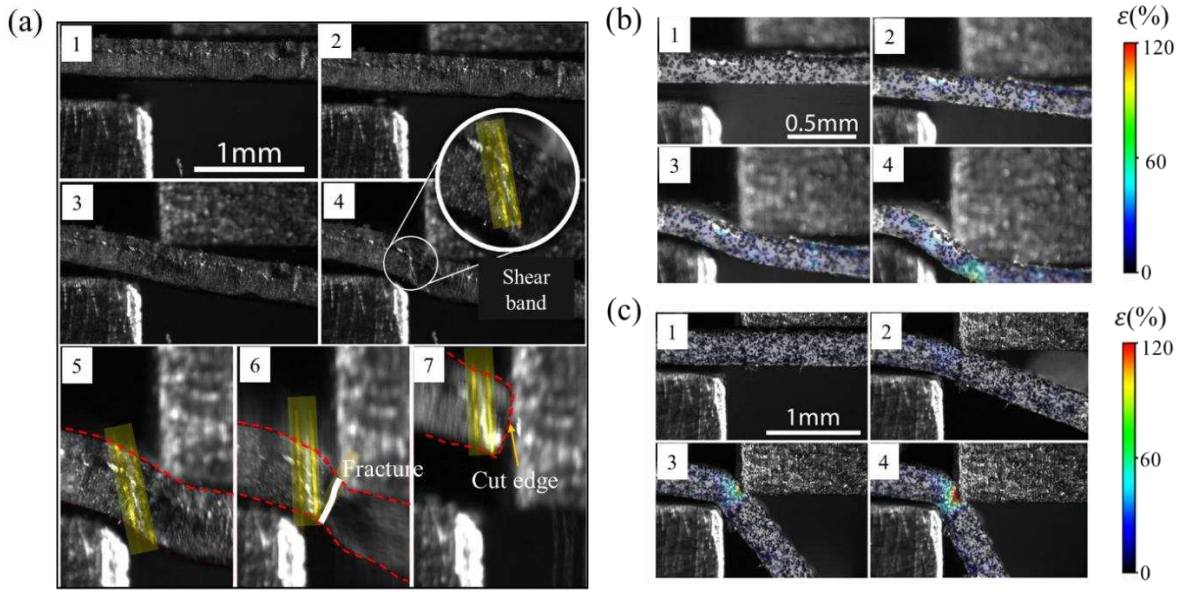


**Fig. 7: (a)** Sequence of frames captured throughout the punch stroke, illustrating the progression of deformation during the blanking process. A shear band forms just prior to fracture, as highlighted in the magnified inset enclosed by yellow lines **(b)** in-situ strain distribution for a 0.2 mm thick sheet, and **(c)** corresponding strain distribution for a 0.35 mm thick sheet, both under single-edge cutting.

SEM micrographs of the blanked sample with 0.2mm thickness at various speed are presented in Fig. 8(a). As the blanking speed increases from 100 to 1000 mm/min, the proportion of the shear zone relative to the fracture zone decreases. This indicates deeper punch penetration into the material, i.e. ductile shearing, at lower speed and ductile fracture at higher speeds. This observation implies that at higher blanking speeds, the sheet material tends to fail more rapidly, likely due to accelerated crack propagation. The burnished or sheared zone is formed entirely through plastic deformation. Following the formation of the burnished zone, the material is subjected to a combination of shear and tensile stresses, which leads to crack initiation and ultimately the formation of the fracture surface, resulting in a rougher surface texture due to material separation. Several features such as micro-cracks, voids and plastic shear bands are observed at the fracture (Fig. 8(b)). The figures also highlight the presence of voids formed during the final stages of blanking, when the material undergoes a mixed tensile–shear failure mode. The concentration of these voids appears to increase near the burr zone.

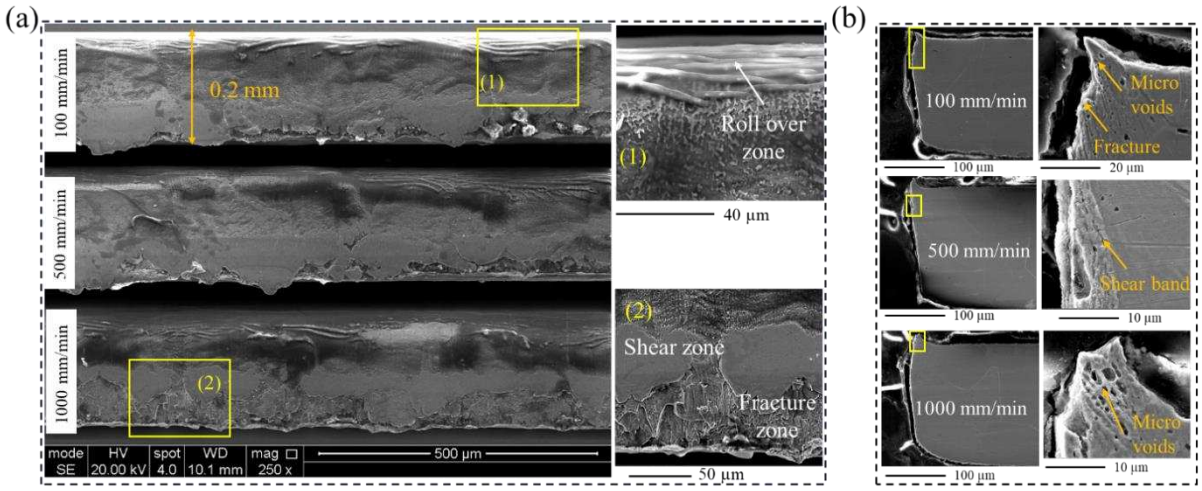


**Fig. 8: (a)** SEM images of blanked cut edges in 0.2 mm thick samples processed at different blanking speeds: 100 mm/min, 500 mm/min, and 1000 mm/min. The micrographs include high-magnification views of selected regions labelled (1) and (2) highlighting microstructural features at the rollover, shear, and fracture zones **(b)** cut-edge fracture surfaces corresponding to each blanking speed, illustrating the fracture characteristics with processing speed.

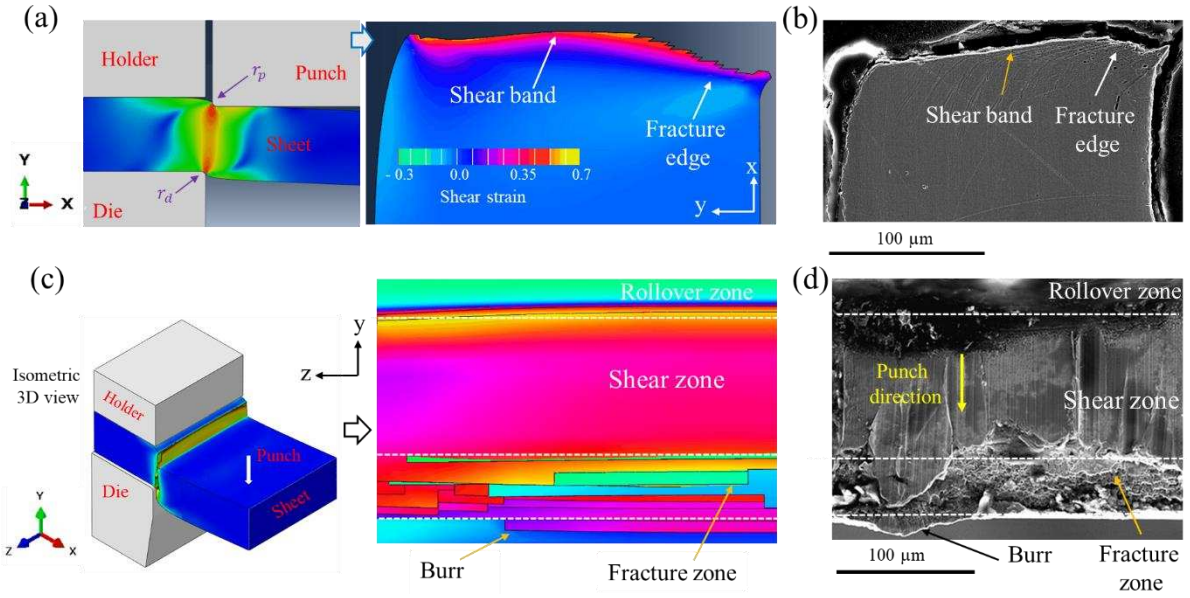


**Fig. 9:** Comparison between simulation and experimental results for the blanking of thin sheet material **(a)** FE simulation showing shear strain distribution across the cut edge, and the fracture edge **(b)** experimentally observed shear bands and fracture patterns **(c)** FE and **(d)** SEM images of the cut edge showing key morphological features, including the rollover zone, shear zone, and fracture surface

FE simulation results are validated against the deformation features, and the cut edge dimensions with SEM images of the actual blanked edges shown in Fig. 9(a, b). The simulated shear strain distribution showed a clear shear band extending from the punch–sheet interface to the fracture edge. The model accurately captured key features such as the rollover zone, shear bands, and transition from plastic shearing to tensile fracture edge morphology, as

highlighted in Fig. 9(c,d), which is critical for assessing cut quality and tool wear. The shear zone length was compared and showed good agreement with experimental results with a difference of less than 10%. Overall, the subroutine-based material model proved effective in simulating high strain-rate blanking, offering reliable predictions of fracture behaviour and edge quality.

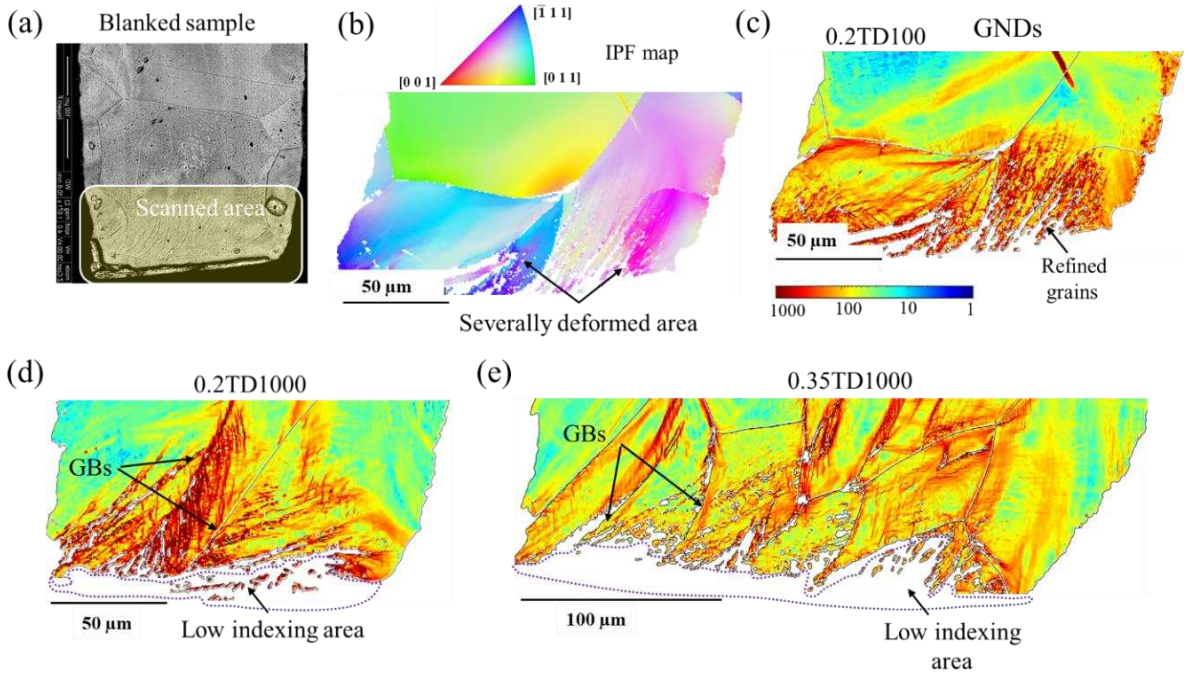


**Fig. 10: (a)** Measurement domain at the cut edge of the sample **(b)** EBSD-scanned inverse pole figure (IPF) distribution of NGO Si-steel; GND distribution at the blanked edge for **(c)** 0.2 mm sheet thickness at a blanking speed of 100 mm/min, **(d)** 0.2 mm thickness at an increased blanking speed of 1000 mm/min, and **(e)** 0.35 mm thickness at 1000 mm/min.

As described previously, the GND distribution is critical to local magnetic performance after blanking. Fig. 10 demonstrates the measured EBSD-scanned IPF and GND distribution at the cut edge of samples cut in the TD direction at various blanking speeds. Severe deformation observed at the cut edge led to grain refinement due to high strain and strain rates (Figs. 10(a, b). The IPF map (Fig. 10(b)) shows the grain orientations relative to the sample frame and highlights microstructural changes from blanking, including grain refinement and localised deformation. The colours indicate crystallographic orientations, allowing visualisation of grain rotation and deformation during cutting. The GND maps reveal substantial deformation at the cut edge, with an increased dislocation density to accommodate the applied plastic deformation at higher cutting speeds revealed in Figs. 10(c,d). The thicker sheet exhibits a lower dislocation density. In contrast, thinner sheets, where only two grains typically span the thickness, must accommodate the applied stresses within a limited structure. Fewer dislocations are observed in the thicker samples, suggesting a slightly smaller degree of deformation within individual

grains. This is attributed to the presence of a greater number of grains sharing the load during deformation, as illustrated in Fig. 10(e).

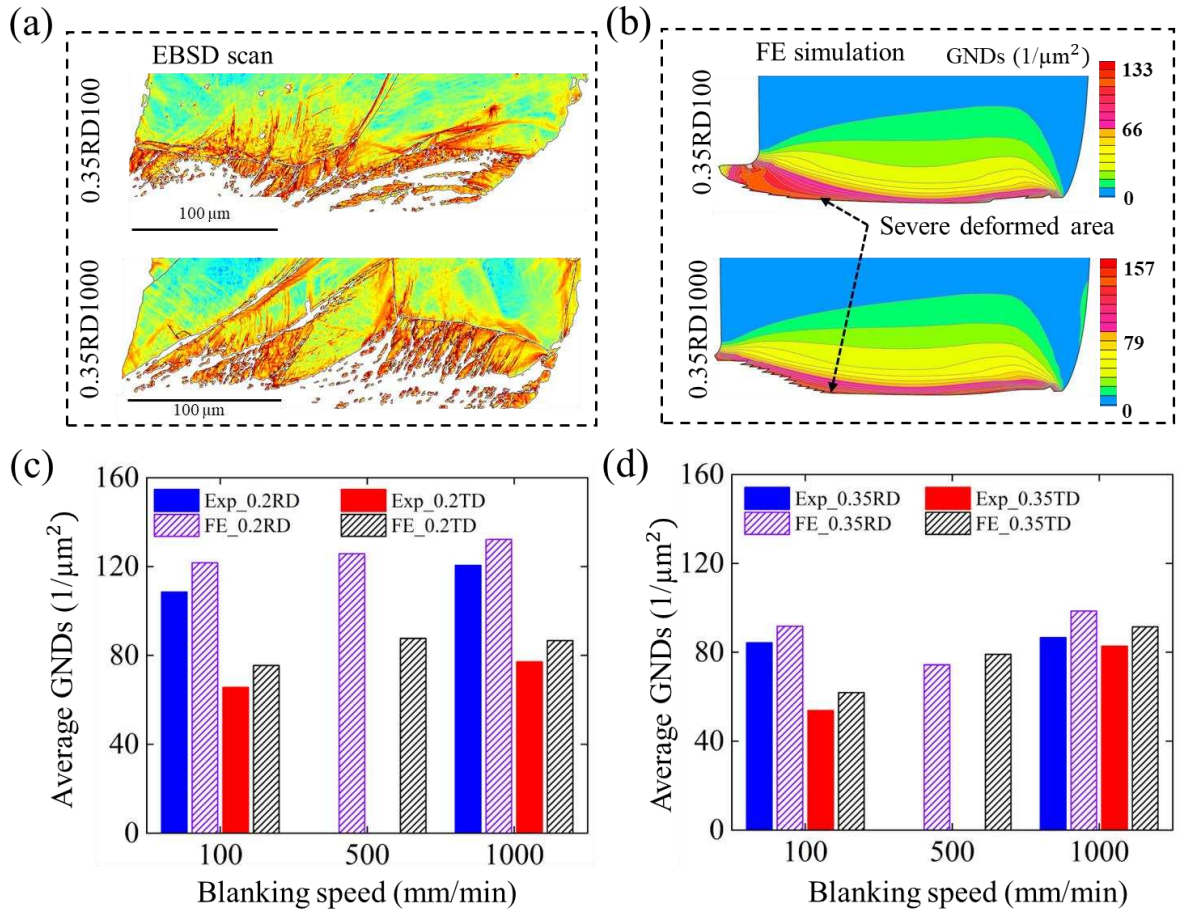


**Fig. 11: (a)** EBSD-derived GND density maps for sheet thicknesses of 0.35 mm, highlighting GND accumulation near the cut edge for cutting speeds of 100 and 1000 mm/min **(b)** FE simulations showing GND distributions, providing deformation behaviour where experimental data is scarce **(c)** quantitative comparison of GND densities obtained from experiments and simulations at thicknesses of 0.2 mm and **(d)** 0.35 mm, across three cutting speeds.

Fig. 11 shows that the predicted GND distributions compared with measured experimental data reported in [42]. Heavily localised large deformation near the cut edge resulted in the lack of precise EBSD indexing and low pattern quality, as shown in the representative GND maps (Fig. 11(a)). In contrast, the FE simulation offers a distinct advantage by enabling estimation of GND magnitudes directly at the cut edge in Fig. 11(b), where experimental techniques are limited. The measured (solid bars) and predicted (hatched bars) GND densities in both the rolling (RD, blue coloured) and transverse direction (TD, red coloured) for sheet thicknesses of 0.2 mm and 0.35 mm are compared in Figs. 11(c,d) respectively. It is worth noting that the experimental data were only available for high and low blanking speeds, and the results for 500 mm/min are only presented from the simulation data. The modelling results consistently overpredicts the

GND densities, with a maximum error of 14% achieved across all conditions that could be attributed to anisotropic deformation behaviour near grain boundaries. Although GND may be higher locally between grains (Fig. 10), these high values occur only in limited regions and do not significantly affect the element-averaged GND, or the overall deformation response captured by the continuum model. Hence, the current simulation may have minor deviations at the local scale due to microstructural heterogeneity, but it is adequate for predicting the overall trend and averaged response.

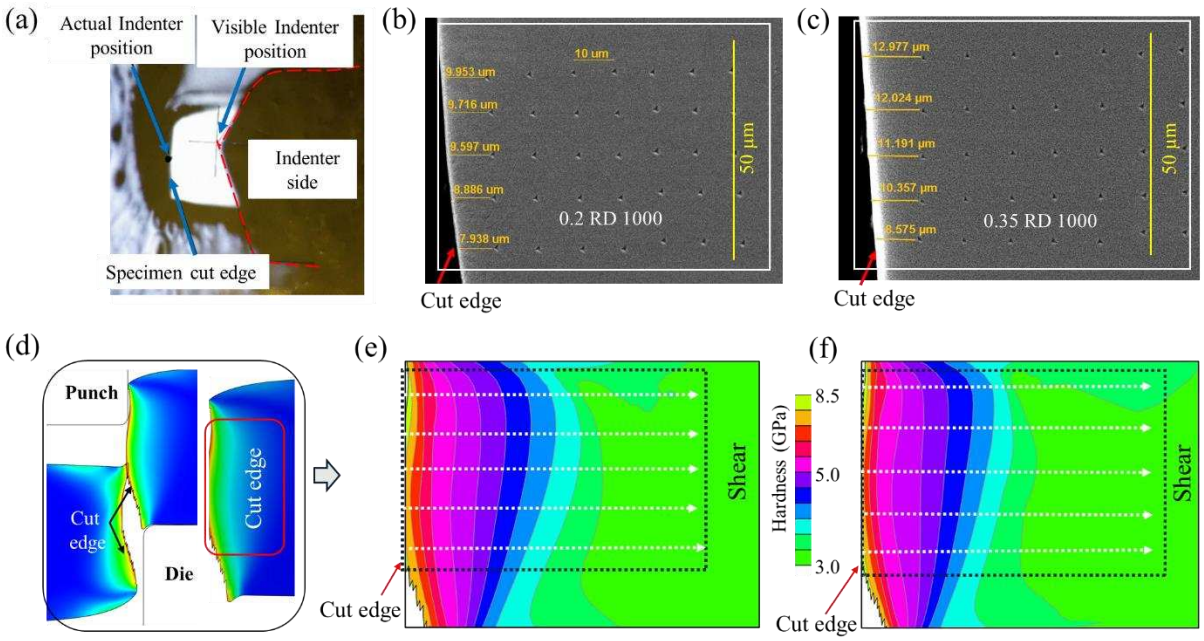


**Fig. 12: (a)** Nano-indentation used for nano-hardness assessment on the cut surface; at two sheet thicknesses **(b)** 0.2 mm and **(c)** 0.35 mm, measured along the rolling direction **(d)** finite element simulation of the cut edge highlighting the region of interest; hardness data were extracted along the white dashed line within the shear-dominated zone for **(e)** 0.2 mm and **(f)** 0.35 mm sheet thicknesses.

As indicated in section 2.2.4, hardness is one of the key variables that can be used to validate material response and provide a link to magnetic performance. Therefore, it was also used as a validation criterion for the developed FE models. The positioning of the nano-indenter probe at the cut edge for nano-hardness assessment is illustrated in Fig. 12(a). The nano-hardness values measured at defined distances from the cut edge for sheet thicknesses of 0.2 mm and 0.35 mm, respectively, along the rolling direction (Figs. 12(b,c)). Indentation points were selected at locations where consistent measurements could be obtained, avoiding the immediate vicinity of the cut edge due to surface curvature and irregularities caused by cutting-induced damage. These measurements are confined to the sheared zone to evaluate the influence of shear deformation identified as the primary mechanism affecting both hardness and dislocation

interactions. Correspondingly, the sheared region at the cut edge was identified within the finite element simulations, shown in Fig. 12(d), and hardness values were extracted along a defined path within this zone for both thicknesses, as illustrated in Figs. 12(e, f).

The comparison between the experimental and simulation results are presented in Fig. 13. The experimental data are shown by triangular markers, and the predicted values are shown by diamond markers, respectively. The simulated hardness values, indicate that intense shear deformation leads to dislocation build-up, increasing the material resistance and resulting in greater hardness. This elevated hardness (7–8 GPa) in the vicinity of the cut edge is observed for both the sheet thicknesses and can be attributed to high dislocation densities and strain hardening, as previously identified in the GND density maps in Fig. 11. In contrast, the lowest hardness values are found near the outer boundary of the deformation zone, where the material properties are closer to those of the undeformed base material. For comparison, the average hardness of the unaffected sheet material, as provided in the simulation and measured in [42, 45] away from the cut edge, ranges between 3.0 and 3.5 GPa. Additionally, the maximum hardness at the cut edge is lower under high-speed blanking conditions (1000 mm/min), as shown in Figs. 13(a, c) and 13(d, f).

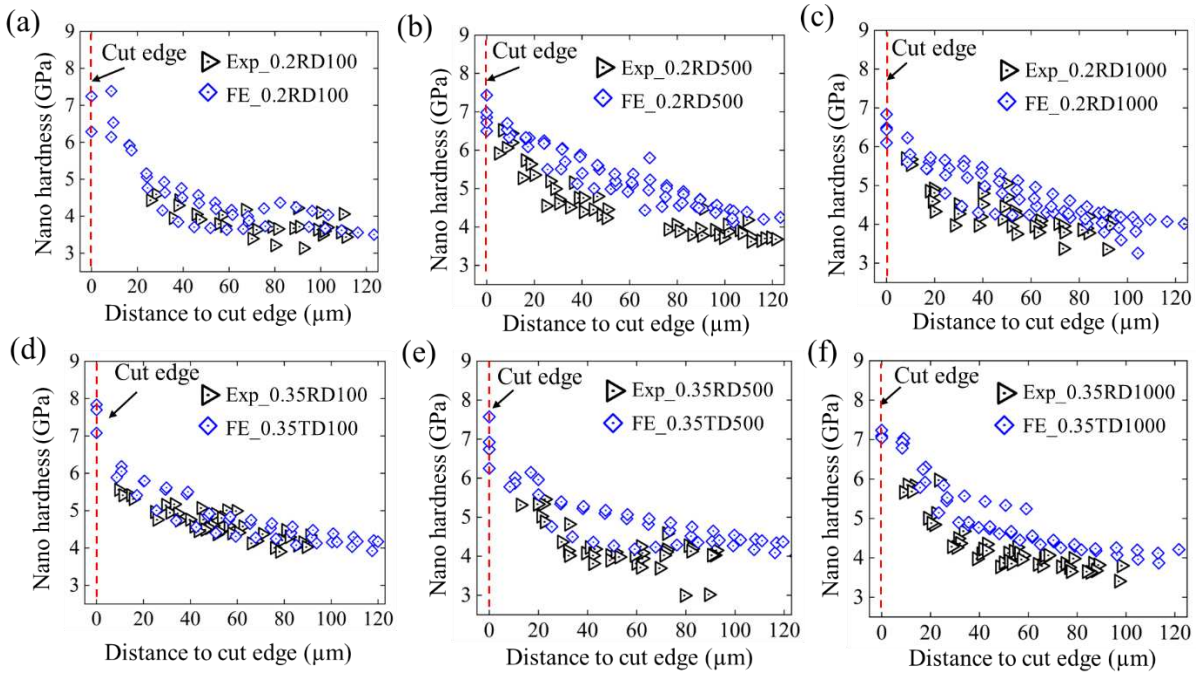


**Fig. 13:** Distribution of nano-hardness values as a function of distance from the cut edge for sheet thicknesses of 0.2 mm and 0.35 mm, tested in the rolling direction (RD) at cutting speeds of **(a, d)** 100 mm/min, **(b, e)** 500 mm/min, and **(c, f)** 1000 mm/min.

A similar hardness trend is observed along the transverse direction, although the absolute values vary, as illustrated in Fig. 14. Nanoindentation measurements were performed at regular

intervals. The data obtained between 60 µm and 80 µm depth in Fig. 14(f) showed some inconsistencies that did not represent the true behaviour of the material. These deviations were most likely due to localised material heterogeneity, minor surface imperfections that affected measurement accuracy. The experimental setup was carefully calibrated and validated on multiple samples, and the remaining data demonstrate consistent trends. To ensure the reliability and integrity of the results, the data points in this range were excluded from the analysis. The remaining data exhibit a consistent trend and reliably capture the mechanical behaviour of the material. The differences between the simulated and measured hardness values may be due to certain limitations in the simulation, such as simplifications in the material model and the mesh resolution, which may affect how accurately localised deformation and hardening are captured.

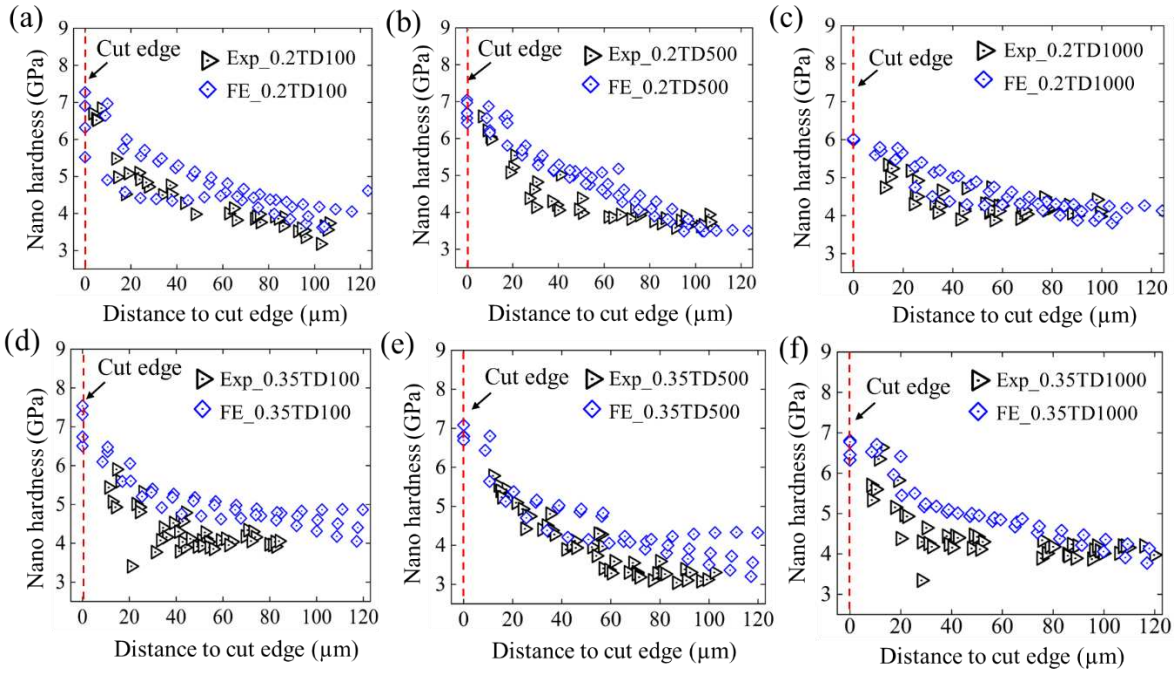


**Fig. 14:** Distribution of nano-hardness values as a function of distance from the cut edge for sheet thicknesses of 0.2 mm and 0.35 mm, tested in the transverse direction (TD) at cutting speeds of **(a, d)** 100 mm/min, **(b, e)** 500 mm/min, and **(c, f)** 1000 mm/min.

The blanking process involves complex deformation mechanisms that lead to the development of residual stresses within the blanked component. Upon initial contact, the punch exerts a concentrated downward force on the sheet material, inducing compressive stresses directly beneath the punch (Fig. 15(a)), while tensile stresses arise in the surrounding area to maintain force equilibrium (Fig. 15(b)). Similar observations were reported by Yasutomi [63]. The compressive loading is essential for initiating plastic deformation. As the punch penetrates further, the material undergoes significant shear deformation, resulting in localised plastic flow.

Following separation, the material adjacent to the sheared edge undergoes elastic recovery (spring back) as external forces are removed. However, this recovery is constrained by the surrounding plastically deformed regions, leading to an incomplete relaxation of stresses. The resulting mismatch between elastic and plastic zones gives rise to tensile residual stresses near the sheared edge shown in Fig. 15(c). These stresses are primarily attributed to the release of prior compressive and shear stresses, the presence of plastic strain gradients, and the influence of punch–die clearance. Fig. 15(d) presents the variation of residual stress along the longitudinal direction from the cut edge for a sheet thickness of 0.35 mm. Tensile residual stress is observed at the sheared surface, which gradually transitions to compressive stress with increasing distance from the edge. This reduction in magnitude is attributed to diminishing plastic strain effects. Notably, as shown in Fig. 15(e), residual stress also varies through the sheet thickness due to the involvement of distinct cutting mechanisms. In the roll over zone, stresses increase due to bending; in the shearing zone, they peak as a result of intense plastic deformation; and finally, they decrease again in the fracture zone.

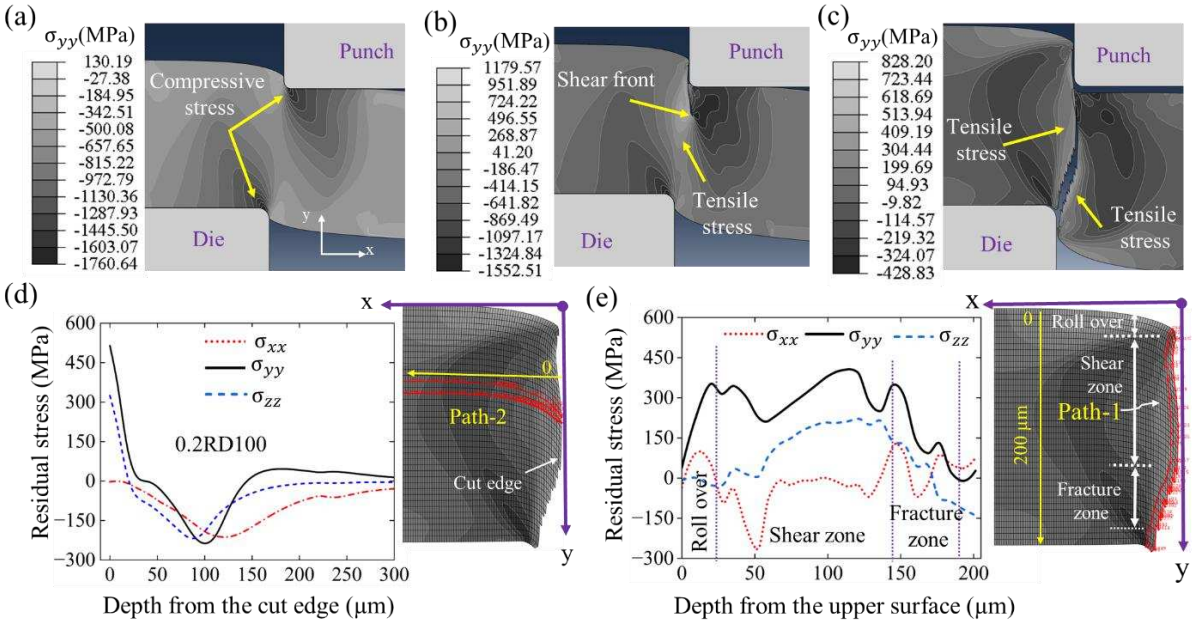


**Fig. 15:** Induced stresses at various stages of the blanking process for a 0.35 mm thick sheet: **(a)** Initial compressive loading **(b)** shearing stage, where the formation of the shear zone is evident **(c)** post-fracture stage, showing residual stress induced at the cut edge **(d)** distribution of residual stress as a function of distance from the cut edge along the longitudinal direction **(e)** distribution of residual stress through the thickness of the sheet.

The extent of deformation leading to residual stress is primarily influenced by the magnitude of plastic strain. The depth of the plastically deformed region was simulated and validated with measurement using DIC following the cutting process. Figs. 16(a) and 16(b) illustrate the blanking of thin sheets with thicknesses of 0.2 mm and 0.35 mm, respectively. In these figures,

red contours indicate zones of localised deformation, blue regions correspond to undeformed areas, and green denotes zones of intermediate deformation. The predicted deformation regions by the developed model under different sheet thickness and the blanking speed is compared with the experimentally measured data in Figs. 16(c) and 16(d). At higher blanking speeds, the depth of deformation was observed to be lower. This reduction is attributed to the formation of a narrower shear zone during high-speed blanking of thin sheets, which consequently results in a reduced extent of plastic deformation.

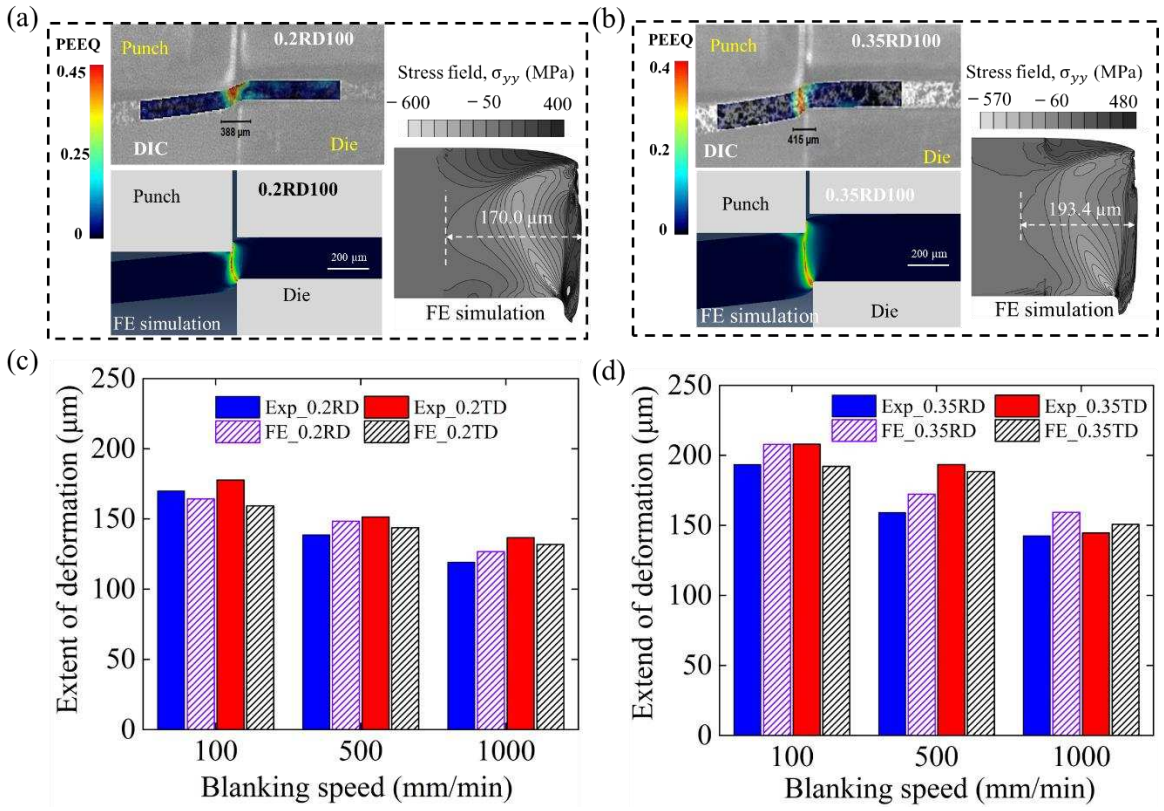


**Fig. 16:** In-situ DIC image of the blanking process, alongside the corresponding FE simulation just prior to fracture, and showing the residual stress distribution within the deformation-affected region; **(a)** for a 0.2 mm sheet **(b)** for a 0.35 mm sheet oriented in the rolling direction **(c)** comparison between the extent of the deformation zone measured by DIC and that predicted by FE simulation for different blanking speeds in the 0.2 mm sheet **(d)** corresponding comparison for the 0.35 mm sheet, evaluated in both the rolling and transverse directions.

The preceding analysis focused on a detailed investigation of the deformation characteristics resulting from blanking of electrical-grade NGO 3.2% silicon steel. In the following section, the influence of such intense plastic deformation arising from different mechanisms on the magnetic performance is examined, with the aim of enhancing the functional properties of the electrical material.

### *3.3 Influence of plastic deformation on magnetic behaviour*

The effect of applied tensile displacement on magnetic relative permeability, shown in Figs. 17(a–e), was investigated for sheet specimens with thicknesses of 0.2 mm and 0.35 mm in both the rolling and transverse directions. For the 0.2 mm sheet, deformation is shown up to a displacement of 5 mm, just prior to fracture, in both rolling and transverse directions (Figs. 17(a) and (b)). A similar analysis for the 0.35 mm sheet is presented in Figs. 17(d, e) up to a displacement of 6 mm. For both sheet thicknesses, the relative permeability curves, measured at a magnetic field strength of 200 A/m, show a clear decrease in magnitude with increasing elongation and corresponding true strain, as illustrated in Figs. 17(c) and (f). This behaviour indicates that domain wall motion is progressively hindered by the introduction of dislocations and residual stresses during plastic deformation.

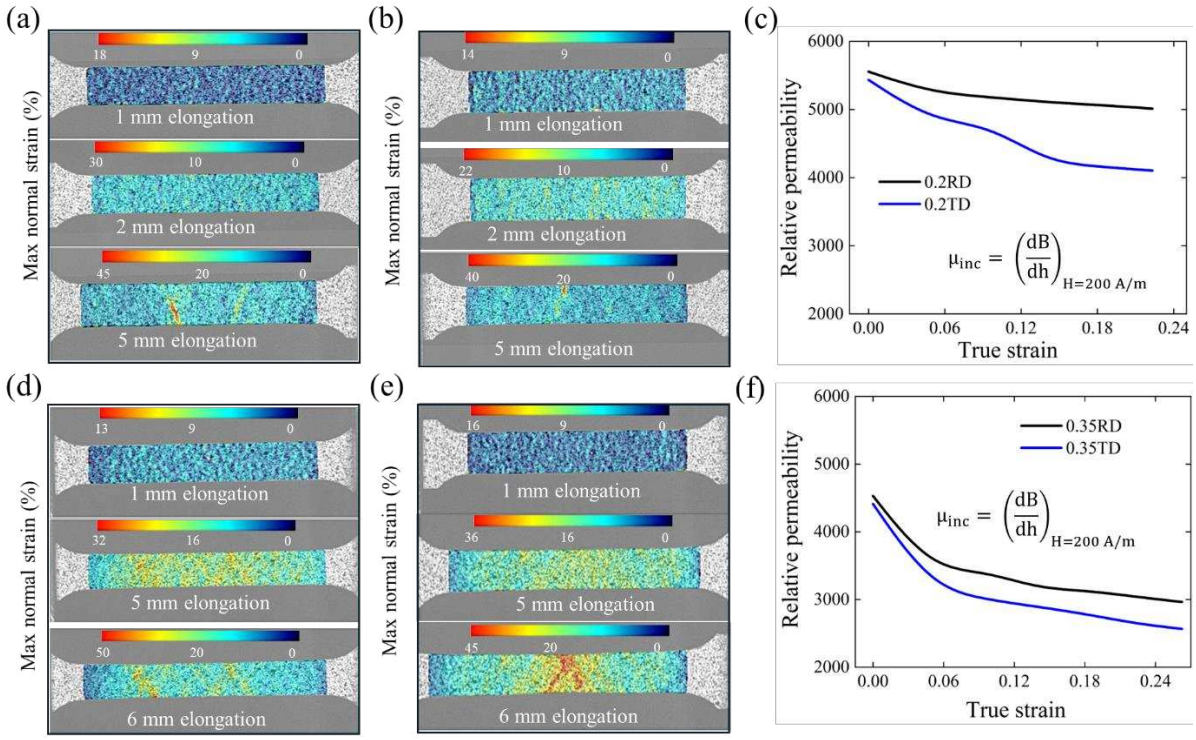


**Fig. 17:** Maximum normal strain distribution in the deformed 0.2 mm thick sample under uniaxial loading: **(a)** rolling direction and **(b)** transverse direction; **(c)** variation of relative permeability with true strain for the 0.2 mm thick sample corresponding to progressive displacement up to 5 mm. Maximum normal strain distribution in the deformed 0.35 mm thick sample under uniaxial loading: **(d)** rolling direction and **(e)** transverse direction; **(f)** variation of relative permeability with true strain for the 0.35 mm thick sample corresponding to progressive displacement up to 6 mm.

The 0.35 mm thick sheets exhibited slightly more pronounced reduction of permeability at a given magnetic field strength, suggesting a greater sensitivity to plastic strain, likely due to a higher number of grains and grain boundaries, which introduce microstructural inhomogeneity.

Overall, these results demonstrate that plastic deformation adversely affects magnetic behaviour, with implications for the mechanical processing and operational performance of electrical steels in applications where both mechanical and magnetic integrity are critical. In and of itself, this general observation is already widely recognised and understood [64, 65], but the results presented in this section provide quantitative support to the understanding of this behaviour.

Fig. 18(a) shows the cut-edge conditions after blanking of the 0.2 mm sheet at different cutting speeds, where shear bands, fracture zones, and micro-cracks are observed. Fig. 18(b) shows, material exhibits steep magnetisation curves and narrow hysteresis loops before cut, indicating low coercivity. After blanking, the hysteresis loops become more inclined with a reduced magnetic flux density at a given field strength. Higher magnetic field strength is required to reach the same saturation level (1.4 T) in the cut specimens, indicating increased coercivity and reduced magnetic permeability. For the 0.2 mm sheet, the coercivity increased from 51.4 A/m to 70.4 A/m, contributing to a 37% rise, while the relative permeability decreased by 19%. Similarly, for the 0.35 mm sheet, coercivity increased by only 13%, and relative permeability reduced by 11%, as the deformation per grain is lower due to the presence of more grains.

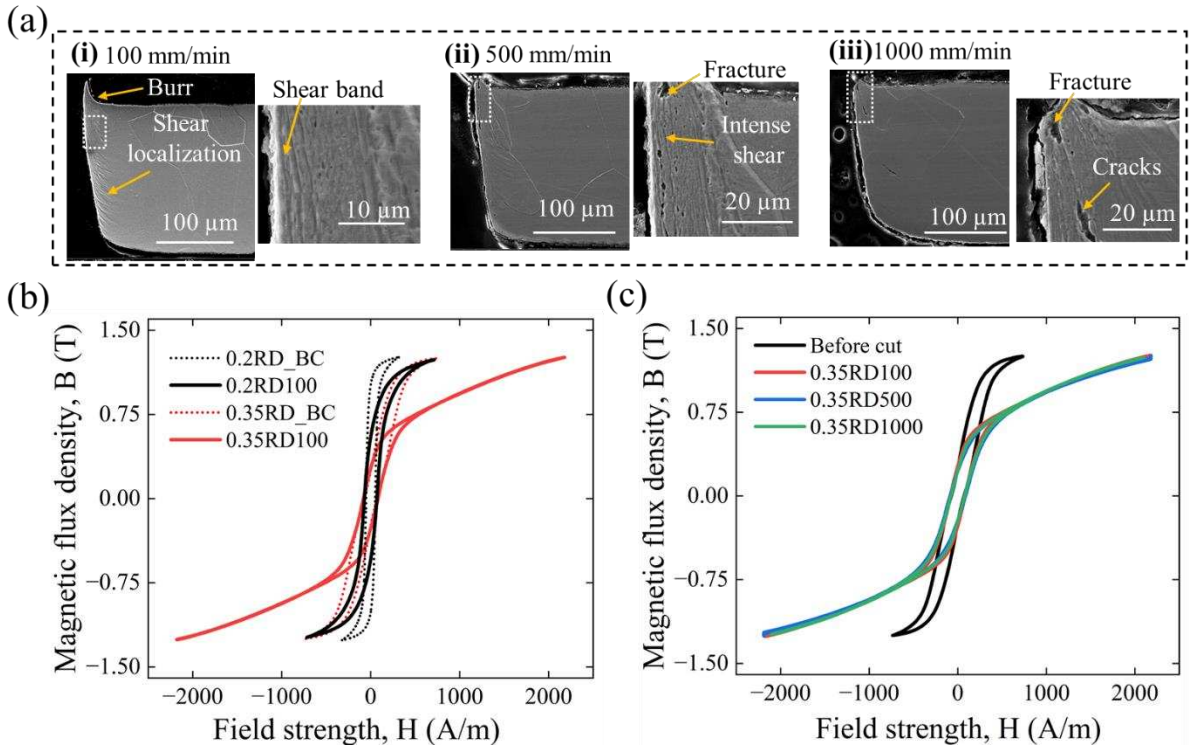


**Fig. 18: (a)** Cut-edge morphology of blanked 0.2 mm Si–steel sheets at different cutting speeds (i-iii), showing shear deformation. fracture and crack initiation; **(b)** B–H hysteresis loops of 0.20 mm and 0.35 mm sheets before and after blanking at 50 Hz; **(c)** effect of cutting speed on the B–H behaviour of the 0.35 mm sheet under constant saturation conditions in the rolling direction.

For the 0.35 mm sheet, the post-blanking B–H curve becomes sharper beyond 1000 A/m (Fig. 18(b)), resulting in a smaller hysteresis loop area in the high-field region. This indicates that, although cutting-induced stresses reduce permeability, the thicker sheet approaches the imposed saturation limit more effectively at higher excitation levels, leading to lower incremental hysteresis loss compared to the 0.20 mm sheet. The degradation in magnetic properties is mainly attributed to the shearing-induced plastically deformed zone near the cut edge (Fig. 18(a)), characterised by high dislocation density, residual stresses, and microstructural damage. Fig. 18(c) shows that for the 0.35 mm sheet under different cutting speeds, all post-blanking cases exhibit a consistent degradation in magnetic performance compared to the uncut state. Although the overall shape of the magnetisation curves remains similar, a slight variation in the hysteresis loop area is observed due to differences in cutting rate. At higher blanking speeds, the reduced interaction time between the punch and material may partially limit the extent of plastic deformation, leading to marginal differences in magnetic degradation. However, the results indicate that the dominant mechanism governing magnetic degradation is the introduction of residual stresses and plastic strain during the blanking process, rather than the cutting speed alone.

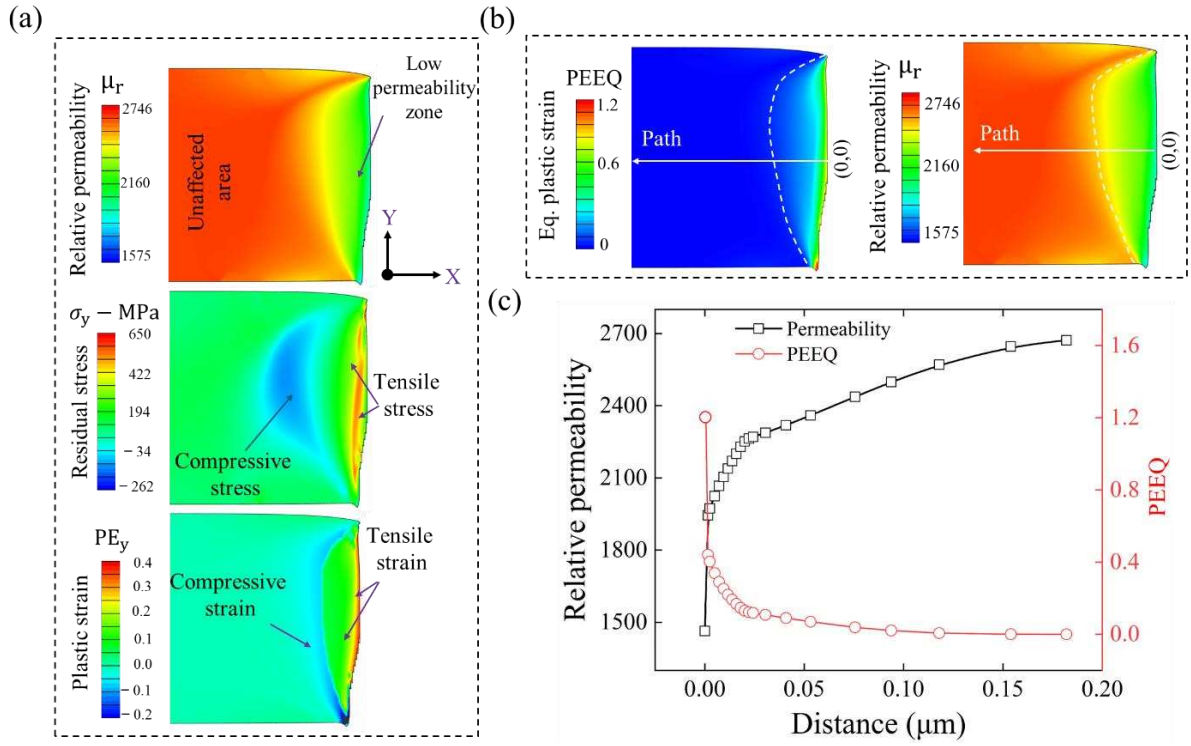


**Fig. 19: (a)** Distribution of stress and strain following blanking, and its effect on the relative permeability of a 0.2 mm-thick sheet oriented in the rolling direction **(b)** path used to trace variable changes from the cut edge along the longitudinal direction **(c)** change in relative permeability as a function of the equivalent plastic strain caused by the blanking process

716 The distribution of relative permeability, residual stress, and residual plastic strain obtained
717 from Finite Element (FE) simulations is presented in Fig. 19. The results reveal that tensile
718 residual stress is highly localised at the cut edge, while compressive residual stress develops
719 beneath the surface at a certain depth (Fig. 19(a)). It is interesting to note that tensile stress has
720 a more pronounced impact on magnetic permeability, leading to a significant reduction,
721 whereas the effect of compressive stress is comparatively less severe. Similar findings are
722 reported in [66], by which the tensile stress has been shown to degrade magnetic permeability
723 and increase core losses, impede domain wall mobility and intensifies hysteresis loss. The
724 compressive residual stress typically situated deeper within the material restricts domain wall
725 motion by introducing localised pinning sites and increasing dislocation density. This
726 contributes to a general reduction in magnetic permeability and an increase in coercive force
727 [67]. Similar phenomena were also noted by [68], compressive stresses can stiffen the magnetic
728 structure, thereby raising the energy required for domain movement and intensifying magnetic
729 losses. The simulation plots in Figs. 19(b,c) quantitatively support these findings, showing that
730 relative permeability is lowest at the cut edge (where tensile stress is dominant) and gradually
731 improves with increasing distance as the plastic equivalent strain (PEEQ) decreases and the
732 influence of compressive stress diminishes. Overall, the presence of these stress states
733 compromises magnetic performance, particularly near the sheared edges, highlighting the
734 importance of optimised cutting processes and post-treatment methods, such as stress-relief
735 annealing, to restore magnetic uniformity and maintain material efficiency in advanced
736 electromagnetic applications.

737 Fig. 20 illustrates the reduction in magnetic permeability under varying blanking speeds and
738 sheet thicknesses at 200 A/m field strength. The post-cutting permeability was estimated using
739 the developed Eq. 11. For each case, deviations between the simulated and experimental results
740 were recorded and reduction in permeability compared with before cut (BC) samples. For the
741 0.2 mm thick sheets, the simulation results showed very good agreement with the experimental
742 data, reaching about 90% correlation (Figs. 20(a) and (b)). In the case of the 0.35 mm thick
743 sheets, a small deviation of up to 8% was observed (Figs. 20(c) and (d)), which still reflects a
744 strong level of agreement. These minor differences can be attributed to enhanced grain
745 boundary interactions under conditions of high localised strain and higher strain rates. The
746 proposed model, which incorporates the influence of strain, strain rate, geometrically necessary
747 dislocations (GNDs), and temperature, has proven to be a useful approach for quantifying
748 mechanically induced cutting processes. It effectively establishes a correlation between

mechanical deformation and magnetic performance, thereby reinforcing the relationship between processing parameters and electromagnetic properties.

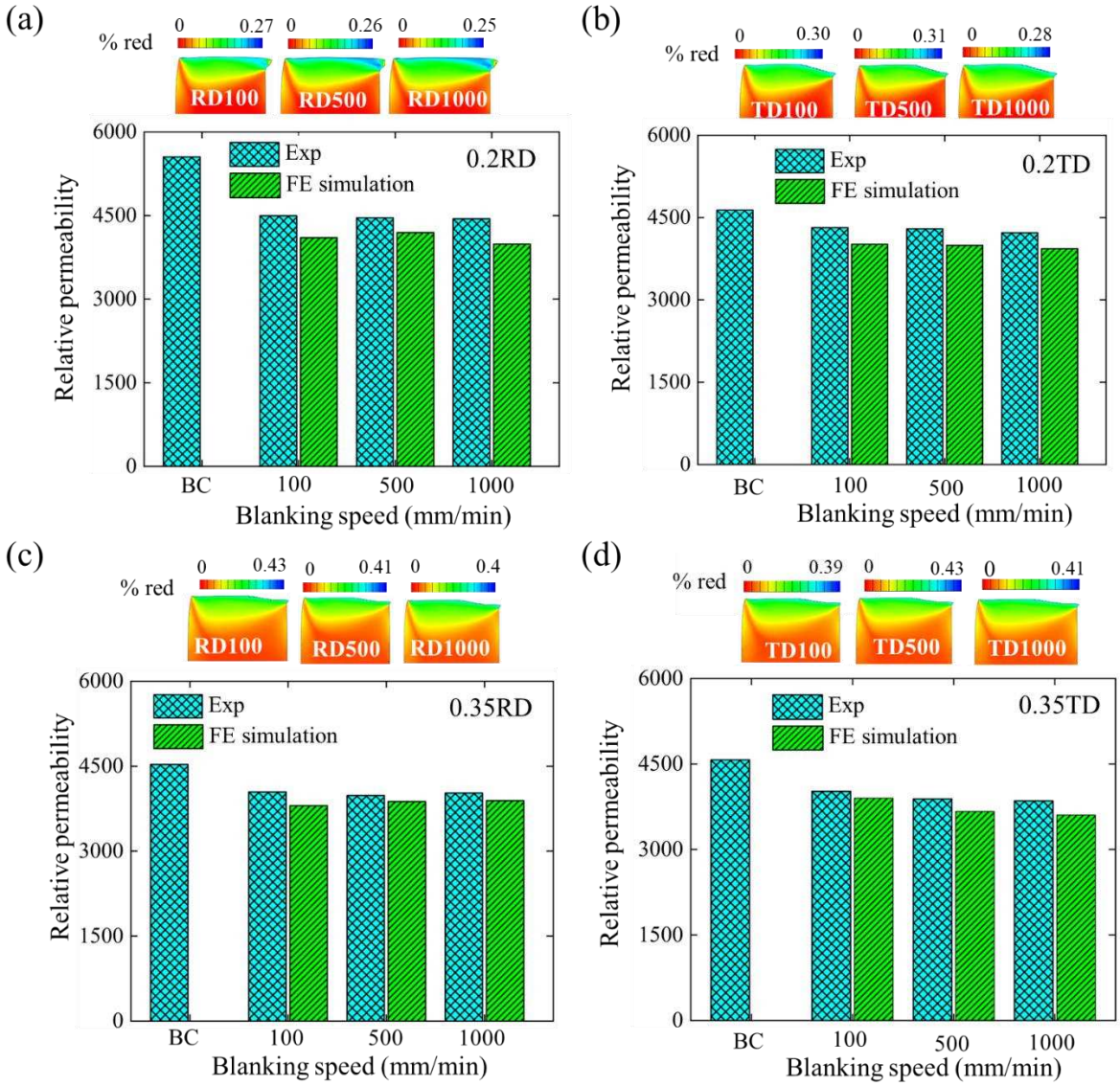


**Fig. 20:** Validation of FE simulations for magnetic permeability at 200 A/m, in electrical steel sheets of varying thicknesses, highlighting the reduction in permeability compared to the pre-cut (BC) state **(a, b)** correspond to the 0.2 mm-thick sheet in the rolling direction (RD) and transverse direction (TD), while **(c, d)** show results for the 0.35 mm-thick sheet in the same orientations.

Fig. 21 illustrates that both the sheet thickness and blanking speed influence on the measured power losses at 50 Hz frequency. Lower losses observed in thicker sheets and at higher cutting speeds. However, the thickness appears to have a more pronounced effect on the measured losses. As previously discussed, thicker samples exhibit less plastic deformation and lower dislocation densities, which result in reduced disturbance to the magnetic domains and, consequently, lower hysteresis losses during magnetisation. Although thinner electrical steel

sheets generally exhibit reduced eddy current losses due to their smaller thickness [69], they can still experience greater overall power losses under certain conditions. At a given magnetic field strength, flux density is generally higher as the sheet gauge size reduces, that could be linked to the effective cross-sectional area of the sheet being tested or a legacy of the additional rolling during manufacture. This elevated flux density for a given magnetic field strength excursion is commonly associated with greater hysteresis losses, as observed in previous research [70], because flux density correlates with the energy absorbed during magnetisation. When domain wall motion is relatively free, less energy is absorbed, leading to lower hysteresis losses. In contrast, mechanical deformation can hinder domain wall motion, necessitating greater magnetic flux and energy input to overcome internal constraints. This results in higher energy dissipation and increased losses.

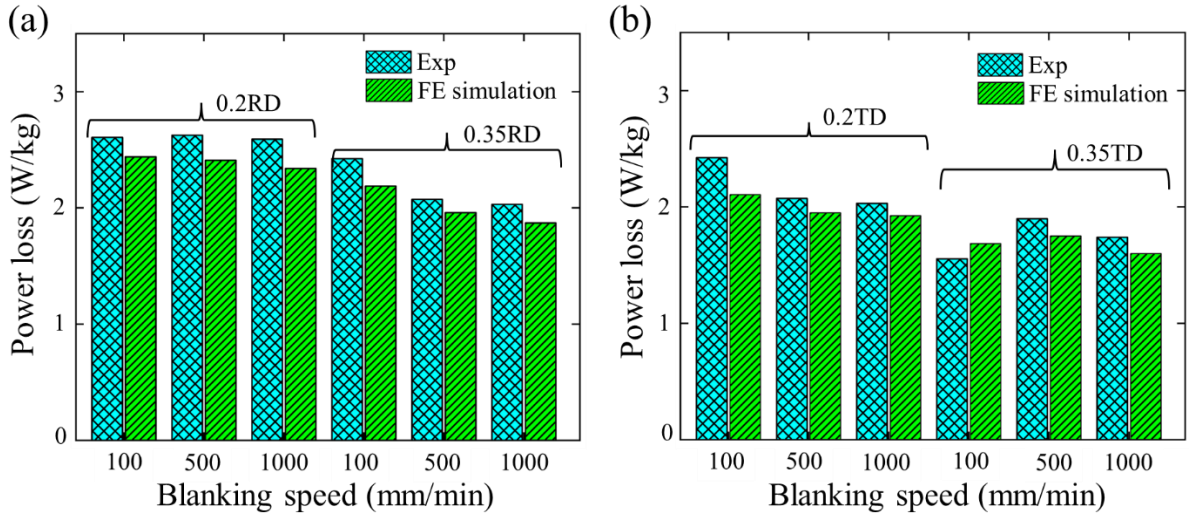


**Fig. 21:** Validation of FE simulations for power loss in electrical steel sheets of different thicknesses, at 50 Hz and 1.4 T **(a)** correspond to the 0.2 mm-thick sheet in the rolling direction (RD) and transverse direction (TD), **(b)** for the 0.35 mm-thick sheet in the same orientations.

The simulated results closely followed the experimental trends, with deviations remaining within 12% (Figs. 21(a,b)). This demonstrates that the proposed modelling approach is sufficiently robust to establish a reliable correlation between mechanical deformation and electromagneticl performance. These findings emphasise the adverse impact of mechanical blanking on the magnetic properties of non-grain-oriented (NGO) steels, underscoring the need to optimise cutting parameters and minimise edge damage in order to maintain performance in electromagnetic applications such as laminates, electric motors and transformers.

## 4. Concluding remarks

The present study systematically proposed a more robust modelling approach to establish a link between plastic deformation during blanking and the resulting magnetic behaviour of electrical steel. The proposed framework advances the current understanding of deformation-induced magnetic responses in non-oriented electrical steels and offers a robust foundation for the predictive design of manufacturing processes where both mechanical integrity and magnetic performance are of critical importance.

It was observed that the number of grains within the cutting vicinity of the blanked edge has a significant influence on the cutting mechanisms. In the case of the 0.2 mm sheet, high GNDs densities were found near the cut edge, as only a small number of grains were available to accommodate the imposed deformation. In contrast, for the thicker 0.35 mm sheet, a greater number of grains contributed to the deformation process, resulting in more distributed strain and consequently lower localised GND densities. This study highlights the presence of non-local deformation at the grain level. Accordingly, the simulation framework was enhanced using a refined flow algorithm that incorporates both grain size effects and non-local deformation characteristics. This allowed for the accurate prediction of GND distributions, including at the cut edge region where experimental measurement remains particularly challenging.

GNDs arise to accommodate strain gradients, particularly in regions experiencing non-uniform plastic deformation such as grain boundaries, interfaces, and cut edges. Their accumulation contributes to localised strain hardening, leading to a notable increase in surface hardness. At the cut edge, the hardness was observed to rise by a factor of 1.2 to 1.6 compared to the bulk material prior to cutting. The simulation successfully captured the nano-hardness trend in good agreement with experimental observations. Residual stress analysis revealed a tensile stress state at the cut edge unfavourable from a mechanical performance perspective, while compressive stress was observed at a short distance away. Higher residual stress was noted within the shear zone due to intense shear localisation and the formation of smooth surfaces, followed by a reduction in the fracture region, attributed to irregular texture and the presence of micro-voids. These findings enhance our understanding of the mechanical and magnetic implications of deformation in precision-cut electrical steels.

This study has demonstrated that plastic deformation induced by the blanking process particularly through intense shearing, leads to dislocation entanglement along grains and grain

boundaries, resulting in pinning effects. This localised residual stresses and strains that impede the movement of magnetic domains during magnetisation. Additionally, the fractured surface exhibited increased roughness due to the formation of micro-voids and tearing, further contributing to domain misalignment. Collectively, these deformation-induced imperfections reduced the magnetic permeability of the material and increased hysteresis losses.

A novel correlation, embedded into equation 11, was proposed between mechanical deformation and magnetic behaviour, allowing magnetic permeability degradation to be predicted with up to 90% accuracy for the 0.2 mm sheet and 92% accuracy for the 0.35 mm sheet. Cut edge damage from blanking increased the coercivity by 37% and 13% for the 0.2 mm and 0.35 mm sheets, respectively. This also led to a reduction in relative permeability of up to 19% for the 0.2 mm sheet and 11% for the 0.35 mm sheet. Furthermore, power loss in thinner sheets (0.2 mm) was observed to be higher for the particular combination of frequency and peak flux density considered, attributed to higher magnetic flux density and increased energy required to overcome internal constraints, resulting in greater energy dissipation and hysteresis losses. The power loss predicted by the proposed model showed good agreement with experimental results, achieving an agreement of 88%. This demonstrates its potential as a reliable design tool for future applications. To enhance the overall efficiency of the process, the design of the die and punch radii was optimised, as well as the clearance, to minimise mechanical damage and ensure smooth cutting, thereby preserving magnetic performance.

Additionally, ongoing work is investigating the effects of specific coating materials on magnetic properties. The current work, while informative, remains limited in scope, and several areas may be explored in future research to enhance predictive capability. Firstly, the incorporation of the Crystal Plasticity Finite Element Method (CPFEM) would enable the modelling of deformation at the grain level, capturing anisotropic plasticity and texture evolution more accurately. Secondly, the development of a fully coupled magneto-mechanical model is recommended, wherein magnetic properties evolve as a function of local stress, strain, and dislocation density. Such an approach would establish a more direct and physically grounded relationship between mechanical deformation and changes in magnetic permeability and associated losses.

**Acknowledgement**

This work is supported by the UK Engineering and Physical Sciences Research Council (EPSRC) through funding for the Future Electrical Machines Manufacturing Hub

(Award EP/S018034/1). The authors also acknowledge the contribution of Dr Ammar Dawood Ghali Al-Rubaye, formerly at University of Sheffield, using experimental data jointly developed by his PhD research.

## References

[1] Nguyen HT, Lin CK, Tung PC, Nguyen VC, Ho JR. Manufacturing motor core lamination from thin non-oriented silicon steel sheet direct by pulsed laser cutting using multi-quality optimized process parameters. *The International Journal of Advanced Manufacturing Technology 2024*; 133, 199–220. https://doi.org/10.1007/s00170-024-13661-1

[2] Petrovic DS. Non-oriented electrical steel sheets. *Mater Tehnol 2010*; 44(6):317–325.

[3] Robert F, Prince A, A R JF. Influence of wire electrical discharge machine cutting parameters on the magnetization characteristics of electrical steel laminations. *Materials Today: Proceedings 2022*; 52 (3): 746-750. https://doi.org/10.1016/j.matpr.2021.10.141

[4] Schoppa A, Louis H, Pude, Rad CV. Influence of abrasive waterjet cutting on the magnetic properties of non-oriented electrical steels. *Journal of Magnetism and Magnetic Materials 2003*; 254(6):370-372. https://doi.org/10.1016/S0304-8853(02)00882-X

[5] Belhadj A, Baudouin P, Breaban F, Deffontaine A, Dewulf M, Houbaert Y. Effect of laser cutting on microstructure and on magnetic properties of grain non-oriented electrical steels. *Journal of Magnetism and Magnetic Materials 2003*; 256: 20-31. https://doi.org/10.1016/S0304-8853(01)00937-4

[6] Steentjes S, Pfingsten GV, Hameyer K. An application-oriented approach for consideration of material degradation effects due to cutting on iron losses and magnetizability. *IEEE Transactions on Magnetics 2014*; 50(11). https://doi.org/10.1109/TMAG.2014.2334699

[7] Emura M, Landgraf F. J. G, Ross W, Barreta J. R. The influence of cutting technique on the magnetic properties of electrical steels. *Journal of Magnetism and Magnetic Materials 2003*; 254-255: 358-360. https://doi.org/10.1016/S0304-8853(02)00856-9

[8] Geiger M, Vollertsen F, Kals R. Fundamentals on the manufacturing of sheet metal microparts. *CIRP Annals 1996*; 45 (1) 277–282. https://doi.org/10.1016/S0007-8506(07)63063-7

[9] Wang GC, Zheng W, Wu T, Jiang H, Zhao G.Q, Wei D.B, Jiang Z.Y. A multi region model for numerical simulation of micro bulk forming. *Journal of Materials Processing Technology 2012*; 212 (3):678–684. https://doi.org/10.1016/j.jmatprotec.2011.05.023

[10] Geibdorfer S, Engel U, Geiger M. FE-simulation of microforming processes applying a mesoscopic model. *International Journal of Machine Tools and Manufacture 2006*; 46 (11):1222–1226. https://doi.org/10.1016/j.ijmachtools.2006.01.019

[11] Paulischin A, Weissitsch L, Wurster S, Fellner S, Krenn H, Bachmaier A. Influence of Severe Plastic Deformation on the Magnetic Properties of Sm–Co Permanent Magnets. *Adv. Eng. Mater 2024*; 26: 2400253. https://doi.org/10.1002/adem.202400253

[12] Kurosaki Y, Mogi H, Fujii H, Kubota T, Shiozaki M. Importance of punching and workability in non-oriented electrical steel sheets. *Journal of Magnetism and Magnetic Materials 2008*; 320(20):2474–2480. https://doi.org/10.1016/j.jmmm.2008.04.073

[13] Weiss H, Leuning N, Steentjes S, Hameyer K, Andorfer T, Jenner S, Volk W. Influence of shear cutting parameters on the electromagnetic properties of non-oriented electrical steel sheets. *Journal of Magnetism and Magnetic Materials 2017*; 421:250–259. https://doi.org/10.1016/j.jmmm.2016.08.002

[14] Nakata T, Takahashi N, Fujiwara K, Nakano M. Study of horizontal-type single sheet testers. *Journal of Magnetism and Magnetic Materials 1994*; 133(1–3):416–418. https://doi.org/10.1016/0304-8853(94)90582-7

[15] Enokizono M, Matsuo H. A measurement system for two dimensional DC-biased properties of magnetic materials. *Journal of Magnetism and Magnetic Materials 2003*; 254:39–42. https://doi.org/10.1016/S0304-8853(02)00747-3

[16] Makar J, Tanner B. The effect of plastic deformation and residual stress on the permeability and magnetostriction of steels. *Journal of Magnetism and Magnetic Materials 2000*; 222(3):291–304. https://doi.org/10.1016/S0304-8853(00)00558-8

[17] Naumoski H, Riedmüller B, Minkow A, Herr U. Investigation of the influence of different cutting procedures on the global and local magnetic properties of non-oriented electrical steel, *Journal of Magnetism and Magnetic Materials 2015*; 392: 126-133. https://doi.org/10.1016/j.jmmm.2015.05.031.

[18] Gomes E, Schneider J, Verbeken K, Pasquarella G, Houbaert Y. Dimensional Effects on Magnetic Properties of Fe–Si Steels Due to Laser and Mechanical Cutting. *IEEE Transactions on Magnetics 2009*; 46(2): 213-216. https://10.1109/TMAG.2009.2034124.

[19] Klingenberg W, Singh U.P. Comparison of two analytical models of blanking and proposal of a new model. *International Journal of Machine Tools and Manufacture 2005*; 45(4–5): 519-527. https://doi.org/10.1016/j.ijmachtools.2004.09.002.

[20] Singh U. P, Klingenberg W, Urquhart W. Effect of Tool Geometry on Punching Performance. *ASME. J. Manuf. Sci. Eng. 1994*; 116(4): 508–513. https://doi.org/10.1115/1.2902135

[21] Mori K, Nakamura N, Abe Y, Uehara Y. Generation mechanism of residual stress at press-blanked and laser-blanking edges of 1.5 GPa ultra-high strength steel sheet. *Journal of Manufacturing Processes 2021*; 68: 435-444, https://doi.org/10.1016/j.jmapro.2021.05.047.

[22] Soyarslan C, Tekkaya A.E. A damage coupled orthotropic finite plasticity model for sheet metal forming: CDM approach. *Computational Materials Science 2010*; 48: 150-165, https://doi.org/10.1016/j.commatsci.2009.12.022.

[23] Rice J.R, Tracey D.M. On the ductile enlargement of voids in triaxial stress fields. *Journal of the Mechanics and Physics of Solids 1969*; 17(3): 201-217. https://doi.org/10.1016/0022-5096(69)90033-7.

[24] Tvergaard V. Material Failure by Void Growth to Coalescence. *Advances in Applied Mechanics 1989*; 27:83-151. https://doi.org/10.1016/S0065-2156(08)70195-9.

[25] Lou Y.S, Huh H. Extension of a shear controlled ductile fracture model considering the stress triaxiality and the lode parameter. *International Journal of Solids and Structures 2013*; 50:447–455. https://doi.org/10.1016/j.ijsolstr.2012.10.007.

[26] Isik K, Yoshida Y, Chen L, Clausmeyer T, Tekkaya A.E. Modelling of the blanking process of high-carbon steel using Lemaitre damage model. *Comptes Rendus Mécanique 2018*; 346(8): 770-778. https://doi.org/10.1016/j.crme.2018.05.003.

[27] Hambli R. Comparison between Lemaitre and Gurson damage models in crack growth simulation during blanking process. *International Journal of Mechanical Sciences 2001*; 43:2769-2790. https://doi.org/10.1016/S0020-7403(01)00070-4.

[28] Mohrbacher H. High-Performance Steels for Sustainable Manufacturing of Vehicles. *Green and Sustainable Manufacturing of Advanced Material 2016*; 135-163, https://doi.org/10.1016/B978-0-12-411497-5.00006-0.

[29] Polatidis E, Haidemenopoulos G.N, Krizan D, Aravas N, Panzner T, Šmíd M, Papadioti I, Casati N, Petegem S. V, Swygenhoven H. V. The effect of stress triaxiality on the phase transformation in transformation induced plasticity steels: Experimental investigation and modelling the transformation kinetics. *Materials Science and Engineering: A 2021*; 800:140321. https://doi.org/10.1016/j.msea.2020.140321.

[30] Papatriantafillou I, Agoras M, Aravas N, Haidemenopoulos G. Constitutive modelling and finite element methods for TRIP steels. *Computer Methods in Applied Mechanics and Engineering 2006*; 195: 5094-5114. https://doi.org/10.1016/j.cma.2005.09.026.

[31] Wieckowski W, Lacki P, Adamus J. Modelling of Fine Blanking Process of the Aluminium Sheets. *Key Engineering Materials 2011*; 473: 290-297. https://doi.org/10.4028/www.scientific.net/KEM.473.290

[32] Soares G. C, Gonzalez B. M, Santos L.D.A. Strain hardening behavior and microstructural evolution during plastic deformation of dual phase, non-grain oriented electrical and AISI 304 steels. *Materials Science and Engineering: A 2017*; 684: 577-585. https://doi.org/10.1016/j.msea.2016.12.094.

[33] Yamasaki T, Yamamoto S, Hirao M. Effect of applied stresses on magnetostriction of low carbon steel. *NDT & E International 1996*; 29(5): 263-268. https://doi.org/10.1016/S0963-8695(96)00028-X.

[34] Wang Z. D, Deng B, Yao K. Physical model of plastic deformation on magnetization in ferromagnetic materials. *J. Appl. Phys. 2011*; 109: 083928. https://doi.org/10.1063/1.3574923

[35] Domenjoud M, Daniel L. Effects of plastic strain and reloading stress on the magneto-mechanical behavior of electrical steels: Experiments and modelling. *Mechanics of Materials 2023*; 176:104510, https://doi.org/10.1016/j.mechmat.2022.104510.

[36] Hubert O, Jendly N, Daniel L. Modelling of the influence of micro plasticity on the magnetic behaviour of ferromagnetic polycrystals through a multiscale approach. *Steel Research International 2016*; 76 (6): 440–447. http://dx.doi.org/10.1002/srin.200506035.

[37] Hubert O, Daniel L. Effect of plastic straining on magnetostriction of ferro magnetic polycrystals–experiments and multiscale modeling. *Journal of Magnetism and Magnetic Materials 2006*; 304 (2): 489–491. http://dx.doi.org/10.1016/j.jmmm.2006.02.132

[38] Pengpeng S. Magneto-elastoplastic coupling model of ferromagnetic material with plastic deformation under applied stress and magnetic fields. *J. Magn. Magn. Mater 2020*; 512:166980. http://dx.doi.org/10.1016/j.jmmm.2020.166980.

[39] Hubert O, Lazreg S. Two phase modeling of the influence of plastic strain on the magnetic and magnetostrictive behaviors of ferromagnetic materials. *Journal of Magnetism and Magnetic Materials 2017*; 424: 421–442. http://dx.doi.org/10.1016/j.jmmm.2016.10.092.

[40] Szumiata T, Rekas P, Gzik-Szumiata M, Nowicki M, Szewczyk R. The Two-Domain Model Utilizing the Effective Pinning Energy for Modeling the Strain-Dependent Magnetic Permeability in Anisotropic Grain-Oriented Electrical Steels. *Materials 2024;* 17(2), 369. https://doi.org/10.3390/ma17020369.

[41] Regan, A., Wilson, J., & Peyton, A. J. Extension to the Jiles–Atherton Hysteresis Model Using Gaussian Distributed Parameters for Quenched and Tempered Engineering Steels. *Sensors 2025;* 25(5), 1328. https://doi.org/10.3390/s25051328.

[42] Ghadbeigi H, Al-Rubaye A, Robinson F.C.J. Hawezy D, Birosca S, Atallah K. Blanking induced damage in thin 3.2% silicon steel sheets. *Prod. Eng. Res. Devel. 2020*; **14**: 53–64. https://doi.org/10.1007/s11740-019-00931-1

[43] Peirs J, Verleysen P, Van Paepegem W, & Degrieck J. Novel pure-shear sheet specimen geometry for dynamic material characterisation. *International conference on the mechanical and physical behaviour of materials under dynamic loading 2009*; 1/2: 35–41. https://doi.org/10.1051/dymat/2009005.

[44] Appino C, Ferrara E, Fiorillo F et al. International comparison on SST and Epstein measurements in grain-oriented Fe-Si sheet steel. *International Journal of Applied Electromagnetics and Mechanics 2015*; 48(2-3):123-133. https://doi.org/10.3233/JAE-151978.

[45] Ghali Al-Rubaye A. D, Characterization of blanking induced magneto-mechanical cut edge defects in non-oriented electrical steel 2019; *Doctoral Thesis, The University of Sheffield. https://etheses.whiterose.ac.uk/id/eprint/24422/*.

[46] Heller M, Stöcker A, Kawalla R, Leuning N, Hameyer K, Wei X, Hirt G, Böhm L, Volk, W, & Korte-Kerzel S. Characterization Methods along the Process Chain of Electrical Steel Sheet—From Best Practices to Advanced Characterization 2022; *Materials*, *15*(1):32. https://doi.org/10.3390/ma15010032.

[47] Hielscher R, Schaeben H. A novel pole figure inversion method: Specification of the MTEX algorithm. *Journal of Applied Crystallography 2008*; *41*(6): 1024–1037. https://doi.org/10.1107/S0021889808030112

[48] Birosca S, di Gioacchino F, Stekovic S, Hardy M. A quantitative approach to studying the effect of local texture and heterogeneous plastic strain on the deformation micromechanism in RR1000 nickel-based superalloy. *Acta Materialia 2014*; 74: 110–124. https://doi.org/10.1016/j.actamat.2014.04.039.

[49] Yadav R, Sharma A, Kulasegaram S, Alimohammadi S, Read D, Brousseau E. Application of mesh-free and finite element methods in modelling nano-scale material removal from copper substrates: A computational approach. *International Journal of Solids and Structures 2024*; 299:112891. https://doi.org/10.1016/j.ijsolstr.2024.112891.

[50] Sunny S, Mathews R, Yu H, Malik A. Effects of microstructure and inherent stress on residual stress induced during powder bed fusion with roller burnishing. International Journal of Mechanical Sciences 2022. 219:107092. https://doi.org/10.1016/j.ijmecsci.2022.107092.

[51] Cheng C, Wan M, Meng B, Zhao R, Han W.P. Size effect on the yield behavior of metal foil under multiaxial stress states: Experimental investigation and modelling. *International Journal of Mechanical Sciences 2019*; 151: 760-771. https://doi.org/10.1016/j.ijmecsci.2018.12.031.

[52] Shen W, Zhanghua C, Chaofang D. Tearing failure of ultra-thin sheet-metal involving size effect in blanking process: Analysis based on modified GTN model. *International Journal of Mechanical Sciences* 2017; 133: 288-302. https://doi.org/10.1016/j.ijmecsci.2017.08.028.

[53] Chen G, Caudill J, Ren C, Jawahir I.S. Numerical modeling of Ti-6Al-4V alloy orthogonal cutting considering microstructure dependent work hardening and energy density-based failure behaviors. *Journal of Manufacturing Processes 2022*; 82: 750-764. https://doi.org/10.1016/j.jmapro.2022.08.032.

[54] Lu X, Zhenyuan J, Haixing Z, Jinhui Q, Yixuan F, Liang S. Y. Simulation of micro-milling inconel 718 considering scale effect. *The International Journal of Advanced Manufacturing Technology 2020*; 108(3): 671-681. https://doi.org/10.1007/s00170-020-05426-3.

[55] Wang S, Chen Z, Dong C. Tearing failure of ultra-thin sheet-metal involving size effect in blanking process: Analysis based on modified GTN model. *International Journal of Mechanical Sciences 2017*; 133: 288-302. https://doi.org/10.1016/j.ijmecsci.2017.08.028.

[56] Yadav R, Chakladar N.D, Paul S. Micro-milling of Ti-6Al-4 V with controlled burr formation. *International Journal of Mechanical Sciences 2022*; 231: 107582. https://doi.org/10.1016/j.ijmecsci.2022.107582.

[57] Yadav R, Chakladar N.D, Paul S. A dynamic recrystallization based constitutive flow model for micro-machining of Ti-6Al-4V. *Journal of Manufacturing Processes 2022*; 77:463-484. https://doi.org/10.1016/j.jmapro.2022.03.040.

[58] Rudnytskyj A, Varga M, Krenn S, Vorlaufer G, Leimhofer J, Jech M, Gachot C. Investigating the relationship of hardness and flow stress in metal forming. *International Journal of Mechanical Sciences 2022*; 232:107571. https://doi.org/10.1016/j.ijmecsci.2022.107571.

[59] Landgraf F.J.G, Emura M. Losses and permeability improvement by stress relieving fully processed electrical steels with previous small deformations. *Journal of Magnetism and Magnetic Materials 2002*; 242–245:152-156. https://doi.org/10.1016/S0304-8853(01)01184-2.

[60] Han B, He Z, Wen T, Zheng S. Design, optimization and test of RHMB considering dynamic characteristics. *International Journal of Mechanical Sciences 2023*; 238: 107847. https://doi.org/10.1016/j.ijmecsci.2022.107847.

[61] Bertotti G, General properties of power losses in soft ferromagnetic materials. *IEEE Transactions on Magnetics 1988*; 24 (621-630). https://doi.org/10.1109/20.43994.

[62] Plotnikov S.M. Determination of Eddy-Current and Hysteresis Losses in the Magnetic Circuits of Electrical Machines. *Meas Tech 2021;* 63 (904–909). https://doi.org/10.1007/s11018-021-01866-9.

[63] Yasutomi T, Yonemura S, Yoshida T, Mizumura M, Hiwatashi S. Blanking Method with Aid of Scrap to Reduce Tensile Residual Stress on Sheared Edge. *J. Phys.: Conf. Ser. 2017;* 896:012098. https://doi.org/10.1088/1742-6596/896/1/012098.

[64] Meijers P.C, Jolink C.T, Tsouvalas A, Metrikine A.V. Magnetic stray field measurements to identify and localise impact-induced plastic deformation in a steel structure. *International Journal of Mechanical Sciences 2022*; 217: 106990. https://doi.org/10.1016/j.ijmecsci.2021.106990.

[65] Sistaninia M, Raninger P, Kreuzer H, Prevedel P, Antretter T. Designing deformation texture in non-oriented electrical steel for enhanced magnetic properties. *International Journal of Mechanical Sciences 2025*; 290: 110090. https://doi.org/10.1016/j.ijmecsci.2025.110090.

[66] Li Y, Song S, Dou Y, Chen T. Influence of tensile stress on the magnetic properties of ultra-thin grain-oriented electrical steel. *AIP Advances 2023*; 13 (2): 025223. https://doi.org/10.1063/9.0000468.

[67] Paulischin A, Weissitsch L, Wurster S, Fellner S, Krenn H, Bachmaier A. Influence of Severe Plastic Deformation on the Magnetic Properties of Sm–Co Permanent Magnets. *Advanced Engineering Materials 2024*; https://doi.org/10.1002/adem.202400253.

[68] Mohan G, Rane R, Kulkarni S.V. Influence of compressive stress on the magnetic characteristics of grain-oriented material under non-sinusoidal excitation. *Journal of Magnetism and Magnetic Materials 2024*; 590: 171148, https://doi.org/10.1016/j.jmmm.2023.171148.

[69] Washko S.D, Miller R.F. Sheet thickness effects on energy losses in 3% silicon-iron. *Journal of Magnetism and Magnetic Materials 1980*; 19:361-364. https://doi.org/10.1016/0304-8853(80)90632-0.

[70] Miyagi D, Aoki Y, Nakano M, Takahashi N. Effect of Compressive Stress in Thickness Direction on Iron Losses of Nonoriented Electrical Steel Sheet. *IEEE Transactions on Magnetics 2010*; 46(6): 2040-2043. https://doi.org/10.1109/TMAG.2010.2042691